UC San Diego

UC San Diego Electronic Theses and Dissertations

Title

Theoretical modeling of signal processing systems in biology

Permalink

https://escholarship.org/uc/item/754196tp

Author

Hu, Bo

Publication Date

2011

Peer reviewed|Thesis/dissertation

eScholarship.org Powered by the California Digital Library
University of California

UNIVERSITY OF CALIFORNIA, SAN DIEGO

Theoretical Modeling of Signal Processing Systems in Biology

A dissertation submitted in partial satisfaction of the
requirements for the degree
Doctor of Philosophy

in

Physics

by

Bo Hu

Committee in charge:

Herbert Levine, Chair
Terence Hwa
José N. Onuchic
Wouter-Jan Rappel
Ruth J. Williams
Jack K. Wolf

2011

Copyright
Bo Hu, 2011
All rights reserved.

The dissertation of Bo Hu is approved, and it is acceptable in quality and form for publication on microfilm and electronically:

_____

_____

_____

_____

_____

_____
Chair

University of California, San Diego

2011

DEDICATION

To my parents.

EPIGRAPH

The laws of physics and chemistry are statistical throughout.

Erwin Schrödinger, 1944

TABLE OF CONTENTS

Signature Page iii

Dedication iv

Epigraph v

Table of Contents vi

List of Figures viii

Acknowledgements ix

Vita and Publications xi

Abstract of the Dissertation xii

Chapter 1 Introduction and Outline 1

Bibliography 4

Chapter 2 Physical Limits of Eukaryotic Gradient Sensing 5
2.1 Introduction 5
2.2 Model and Results 6
2.3 Discussion 13
2.4 Technical Details 15
2.5 Concluding Remarks 17
2.6 Acknowledgements 18

Bibliography 19

Chapter 3 Stochastic Modeling of Eukaryotic Chemotaxis 21
3.1 Introduction 21
3.2 Model 23
3.3 Results 26
3.4 Discussion 32
3.5 Acknowledgements 33

Bibliography 34

Chapter 4 Input Noise in a Biological Switching System 36
4.1 Introduction 36
4.2 Model and Results 37
4.3 Discussion 45

4.4 Acknowledgements 46

Bibliography 47

Chapter 5 Mechanisms for Signaling Specificity 49
5.1 Introduction 49
5.2 Results 50
5.2.1 A four-node module underlies signaling pathways with cross-activation 50
5.2.2 Asymmetric hierarchical inhibition ensures signaling specificity 51
5.2.3 Generalization of our results 55
5.2.4 Application to yeast signaling pathways 57
5.3 Discussion 61
5.4 Materials and Methods 63
5.4.1 The four-node ODE model 63
5.4.2 The network genetic algorithm 64
5.5 Acknowledgements 65

Bibliography 66

LIST OF FIGURES

Figure 2.1: Schematic representation of the gradient sensing model 7
Figure 2.2: Analytical and simulation results for gradient sensing limits. . . 9

Figure 3.1: Schematic representation of our model 22
Figure 3.2: The average speed of chemotactic cells in experiments 24
Figure 3.3: Directional distribution and chemotaxis index for our model . . 27
Figure 3.4: Optimal chemotaxis index and fitting to experimental data . . . 29

Figure 4.1: Analytical and numerical results in the slow switch limit 40
Figure 4.2: Numerical results of our model in the fast switching limit . . . 43

Figure 5.1: A four-node topology underlies cross-activating pathways 52
Figure 5.2: The asymmetric hierarchical inhibition mechanism 54
Figure 5.3: Application of the asymmetric hierarchical inhibition mechanism 60

ACKNOWLEDGEMENTS

This dissertation would not have been possible without the support and help of many people.

Firstly, I would like to express my sincere gratitude and deep appreciation to my advisor, Herbert Levine, for his constant support, encouragement, patience, and mentoring over the last five years of my research. His breadth of mind, deep insight, and wide knowledge has a tremendous impact on every aspect of my academic pursuit. I am also greatly indebted to Wouter-Jan Rappel for his collaboration and guidance. Wouter is always willing to share his expertise and experience with me, and has devoted countless amount of time and energy to help me going through many difficulties.

I am deeply grateful to Terry Hwa, Ruth J. Williams, José N. Onuchic, and Jack K. Wolf for being my mentors and teachers, serving as my committee members, and providing invaluable advices on my research. Terry introduced me into the exciting field of quantitative biology through his wonderful class of statistical biophysics. Almost all my research projects have involved knowledge and techniques I learned from him. Ruth let me constantly appreciate the beauty, rigor, and power of mathematics through her instruction over many years. She is the best math teacher I have ever had, and her door is always open whenever I have questions or need help. José is an admiring role model in science and a great leader who stimulates me to contribute high quality of research. Jack and his wife Toby have been extremely helpful in every aspect of our life since Wen and I first came to US. They selflessly helped us and taught us a lot, especially, how to live a meaningful life.

I would like to thank William F. Loomis, Danny Fuller, David A. Kessler, Bo Li, and Yuhai Tu (IBM) for helping me, collaborating with me, or giving me opportunities and advices at different stages of my studies. It has been my greatest pleasure to work with many wonderful colleagues in the Center for Theoretical Biological Physics, including Wen Chen, Danying Shao, Monica Skoge, Inbal Hecht, Kai Wang, Sichun Yang, Rutger Hermsen, Tony Hui, Anat Burger, Albert Bae, Laura Tucker, Scott Wylie, Suhita Nadkarni, Mathias Buenemann,

Peter McHale, Ting Lu, Shenshen Wang, Daniel Schultz, and so on. Lastly, I would never have accomplished my graduate study without the loving support of my parents throughout.

Chapter 2, in part, is the published material as it appears in Physical Review Letters, (2010), Hu, Bo; Chen, Wen; Rappel, Wouter-Jan; Levine, Herbert. The dissertation author was the primary investigator and author of this paper.

Chapter 3, in part, is the published material as it appears in Physical Review E, (2010), Hu, Bo; Fuller, Danny; Loomis William F.; Levine, Herbert; Rappel, Wouter-Jan. The dissertation author was the primary investigator and author of this paper.

Chapter 4, in full, is the material which has been submitted for publication and which may appear in Physical Review, (2011), Hu, Bo; Kessler, David A.; Rappel, Wouter-Jan; Levine, Herbert. The dissertation author was the primary investigator and author of this paper.

Chapter 5, in part, is the published material as it appears in Physical Biology, (2011), Hu, Bo; Levine, Herbert; Rappel, Wouter-Jan. The dissertation author was the primary investigator and author of this paper.

VITA

2005	B. S. in Physics, University of Science and Technology of China
2007	M. S. in Physics, University of California, San Diego
2011	Ph. D. in Physics, University of California, San Diego

PUBLICATIONS

Bo Hu, Wen Chen, Wouter-Jan Rappel, and Herbert Levine, "How geometry and internal bias affect the accuracy of eukaryotic gradient sensing." *Physical Review E*, **83**, 021917 (2011).

Bo Hu, Wen Chen, Herbert Levine, and Wouter-Jan Rappel, "Quantifying Information Transmission in Eukaryotic Gradient Sensing and Chemotactic Response." *Journal of Statistical Physics*, **142**, 1167, (2011).

Bo Hu, Herbert Levine, and Wouter-Jan Rappel, "Design principles and specificity in biological networks with cross-activation." *Physical Biology*, **8**, 026001, (2011).

Bo Hu, Wen Chen, Wouter-Jan Rappel, and Herbert Levine, "Physical limits on cellular sensing of spatial gradients." *Physical Review Letters*, **105**, 0481041 (2010).

Bo Hu, Danny Fuller, William F. Loomis, Herbert Levine, and Wouter-Jan Rappel, "Phenomenological approach to eukaryotic chemotactic efficiency." *Physical Review E*, **81**, 031906 (2010).

Bo Hu, Wouter-Jan Rappel, and Herbert Levine, "Mechanisms and constraints on yeast MAPK signaling specificity." *Biophysical Journal*, **96**, 4755 (2009).

ABSTRACT OF THE DISSERTATION

Theoretical Modeling of Signal Processing Systems in Biology

by

Bo Hu

Doctor of Philosophy in Physics

University of California, San Diego, 2011

Herbert Levine, Chair

The survival of biological organisms relies on their capacity to sense and respond to various environmental signals. Such capacity is limited by stochasticity of both intracellular and extracellular signaling events and by potential cross-talk of signaling pathways. Understanding the performance of biological signaling networks is essential for a comprehensive explanation of biological mechanisms and functions.

This dissertation presents theoretical models, primarily developed by the dissertation author, for various biological signal processing systems, including eukaryotic gradient sensing, chemotactic response, enzymatic switch system under noisy input, and specificity of yeast signaling networks. In those studies, we have

employed a wide range of concepts and techniques in statistical mechanics, estimation theory, stochastic process, stochastic differential equation, numerical optimization, and Monte-Carlo simulations.

In the analysis of gradient sensing limits (Chapter 2), we found that the accuracy of spatial gradient sensing is highly sensitive to the cell size and that the spatial sensing strategy may also be applicable to some small bacteria with the aid of receptor cooperativity. In the study of chemotactic response (Chapter 3), we developed an exactly solvable model which incorporate different sources of noise and can well explain the experimentally observed heavy-tails in the directional distribution of chemotactic cells. Chapter 4 devotes to the study of a simple biological switching system (e.g., gene promoter and bacterial motor) governed by fluctuating input signals. Our analytical results question the common belief that input noise will always contributes additively to the output variation. Finally, in the context of signaling specificity, we discovered and proposed a general design principle, namely *the asymmetric hierarchical inhibition mechanism*, for signaling pathways to avoid cross-talk and achieve specificity.

Chapter 1

Introduction and Outline

In order to survive and prosper, biological systems have to constantly detect and process various signals arising from their internal and external environments. For example, bacteria, in response to certain chemical signals, move toward food resources. Yeast cells communicate and mate with each other through releasing and sensing specific pheromone molecules. A central question in biophysics is to understand how accurate and reliable the biological signal processing systems are. Answering this question is essential for a comprehensive understanding of biological processes and functions and is instructive for designing novel biological systems. This dissertation is devoted to explore many interesting topics and systems surrounding this question.

The response of cells to external stimuli is often limited by the *randomness* and *interference* of relevant signaling events. First, the birth and death of signaling molecules are stochastic in nature. Second, any biochemical reaction is in principle a stochastic process. Last, although the redundancy of biological networks may increase their robustness, it also brings up the potential problem of cross-talk and loss of signaling specificity. This dissertation focuses more on the first limiting factor, *randomness* or noise. Only in the last chapter, we deal with the second limiting factor, *interference* or cross-talk. This dissertation is composed of four separate research projects, which, however, shares the common theme as I addressed in the beginning. Each project contains a theoretical model as well as computational simulations for a specific signaling system.

In Chapter 2, we explore the physical limits of spatial gradient sensing strategy, using statistical mechanics and estimation theory. The idea is to treat the chemoreceptors for gradient sensing as classic spins subject to a spatially varying magnetic field. By calculating the partition function of the system, we can derive fundamental limits for a cell to measure the gradient steepness and direction. Such limits are placed primarily by the *receptor noise* as the receptor flips its states stochastically. We also extend our simple spin-chain model to an Ising type model by incorporating possible receptor cooperativity. Using statistical perturbation theory and transfer matrix method, we can still evaluate the partition for our Ising system and find all the statistical quantities of our interest. Our results reveal that the precision of spatial gradient sensing not only increases dramatically with the cell size but also can be improved significantly in the presence of receptor coupling. The latter effect may open the possibility for small bacteria to perform the spatial gradient sensing strategy. This chapter is largely based on the publication in *Physical Review Letter* (2010), of which the dissertation author is the primary investigator and author [1].

In Chapter 3, we present a phenomenological Langevin model for chemotactic cells, by incorporating both the *receptor noise*, as discussed in the previous chapter, and the *spontaneous motility noise* independent of the gradient signal. Solving the Fokker-Planck equation, we can find the stationary directional distribution of chemotactic cells. The theoretical distribution fit well to the experimental data for the social amoeba *Dictyostelium* cells from our collaborators. Specifically, both the data and our model exhibit heavy tails in the directional distribution. Such leptokurtic property is absent in a naive model which does not contain the direction-dependent multiplicative noise. The content of this chapter is mostly based on our recent publication in *Physical Review E* (2010), of which I am the primary developer of the model [2].

We discuss, in Chapter 4, a general model of biological switching system governed by a fluctuating input signal. This project is conceived to study the role of input noise in discrete-state biological systems. A biochemical switch can only be in two states, either on or off, at any time. In our model, the input

signal is represented by the amount of molecules generated from a simple birth and death process. This input signal regulates the transition rates of the switch between the on and off states. By solving the joint master equations for the whole system, we find that the conventional *input-output additive noise rule* is not a good characterization of a single switch system, and that the net effect of input noise is to shift the overall probability to find the switch in the on state. This chapter, in full, has been submitted for publication and may appear in Physical Review (2011). The dissertation author is also the primary author of this paper [3].

The last chapter is devoted to the issue of pathway specificity in biological signaling networks. We start from simplifying two cross-talking pathways into a four node model, which can be easily described by four ordinary differential equations. We further employ a modified genetic algorithm to look for all possible network topologies that could exhibit the required specificity after adding various cross-pathway inhibitory links. The optimal solutions we found correspond to a novel mechanism, namely, the *asymmetric hierarchical inhibition*. This mechanism provides a plausible explanation for the puzzle in yeast signaling specificity (mating versus filamentation pathways). Chapter 5 is largely based on the publication in *Physical Biology* (2011), of which the dissertation author is the primary investigator [4].

Bibliography

[1] B. Hu, W. Chen, W.J. Rappel, and H. Levine, Phys. Rev. Lett. **105**, 048104 (2010).

[2] B. Hu, D. Fuller, W.F. Loomis, H. Levine, and W.J. Rappel, Phys. Rev. E **81**, 031906 (2010).

[3] B. Hu, D.A. Kessler, W.J. Rappel, and H. Levine, (in submission).

[4] B. Hu, H. Levine, and W.J. Rappel, Phys. Biol. **8**, 026001, (2011).

Chapter 2

Physical Limits of Eukaryotic Gradient Sensing

2.1 Introduction

Cells often direct their motion under the guidance of chemical gradients. This is essential for critical biological functions including neuronal development, wound repair and cancer spreading [1]. To detect gradients, small organisms like bacterial cells usually employ a temporal sensing strategy by measuring and comparing concentration signals over time along their swimming tracks [2, 3]. In contrast, eukaryotic cells are sufficiently large to implement a spatial sensing mechanism, as they can measure the concentration differences across their cell bodies. Measurements for both strategies are accomplished by specific cell-surface receptors which diffusing chemical particles (ligands) can bind to. Spatial sensing among eukaryotes exhibits a remarkable sensitivity to gradients of merely 1-2% across the cell [4, 5, 6, 7]. Given the dynamic fluctuations in ligand-receptor interaction, the receptor signal is inherently noisy, as demonstrated by single-cell imaging experiments [8, 9]. This naturally raises a question concerning the reliability of spatial gradient sensing.

In analyzing bacterial chemotaxis, Berg and Purcell showed that the minimal uncertainty of concentration sensing is set by the diffusion of ligand particles

[10]. This work has been extended to include ligand-receptor binding effects and possible receptor cooperativity [11, 12, 13, 14, 15, 16, 17]. Instead of measuring the mean concentration, the spatial sensing program concerns the acquisition of information regarding the asymmetry in space (the gradient steepness and direction). Still, the accuracy of gradient measurements must be limited by physical laws governing ligand diffusion and stochastic receptor-ligand dynamics. Previous studies on gradient sensing limits are either based on idealized mechanisms in absence of kinetics [14], or restricted to one-dimensional simplifications in which sensing is a *discrete* choice [17], or rely on heuristic signal transduction models [18, 19]. Thus, the precise attainable accuracy remains unknown for directional sensing. Here, we address this problem more generally using a statistical mechanical approach, where we view the surface receptors as a (possibly coupled) spin chain and treat the chemical gradient as a perturbation field. By calculating the system's partition function, we are able to derive the gradient sensing limits both for independent receptors and for receptors exhibiting cooperativity. Our results lead to the prediction that the spatial sensing strategy may not be exclusive to large eukaryotic cells, but also be applicable to some small bacteria [20], especially with the aid of receptor cooperativity.

2.2 Model and Results

We consider a circular cell with diameter L immersed in a chemoattractant gradient (Fig. 2.1) and suppose that there are N receptors distributed at equally spaced intervals on the cell perimeter. This assumption is for analytical convenience and can be relaxed numerically. Our theoretical results work well even if the receptors are uniformly distributed at random. The angular coordinates of these receptors are indicated by $\varphi_n = 2\pi n/N$ for $n = 1, ..., N$. For analytical convenience, we assume that the gradient field takes an exponential profile, as was recently realized in experiments utilizing the social amoeba *Dictyostelium* [7, 21]. The local concentration at the n-*th* receptor is

$$C_n = C_0 \exp\left[\frac{p}{2}\cos(\varphi_n - \phi)\right], \tag{2.1}$$

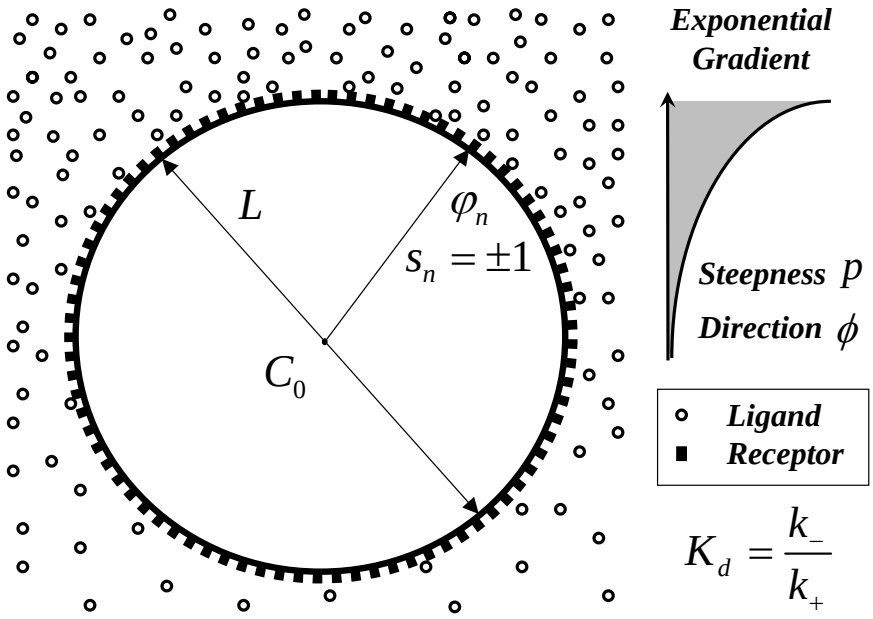


Figure 2.1: Schematic representation of the gradient sensing model: a circular cell, covered with receptors, is placed in an exponential gradient. The forward and backward rates $k_\pm$ control the transition between the bound and unbound states for the receptors.

where C_0 is the background concentration, p denotes the gradient steepness, and ϕ indicates the gradient direction. By its definition, $p \equiv \frac{L}{C_0}|\vec{\nabla}C|$ quantifies the percentage concentration change across the cell length L. Like a spin in physics, each receptor switches between two states: either active ($s_n = +1$) or inactive (-1). For independent receptors, a receptor is activated only if it is bound by ligand and inactive otherwise. Let the energy associated with the state $s_n = +1$ (or -1) be $-\varepsilon_n$ (or $+\varepsilon_n$) in units of the thermal energy k_BT. Then the "on" probability of the n-th spin is given by the Boltzmann distribution: $P_{on} = e^{\varepsilon_n}/(e^{\varepsilon_n} + e^{-\varepsilon_n})$. For simple receptor-ligand kinetics (Fig. 2.1), we have $P_{on} = C_n/(C_n + K_d)$ in chemical equilibrium where $K_d = k_-/k_+$ is the dissociation constant. Thus, the free energy has the expression:

$$\varepsilon_n = \frac{1}{2}\ln\frac{C_n}{K_d} = \frac{1}{2}\ln\frac{C_0}{K_d} + \frac{p}{4}\cos(\varphi_n - \phi) \equiv \alpha_0 + h_n, \tag{2.2}$$

where $\alpha_0 = \frac{1}{2}\ln(C_0/K_d)$ and $h_n = \frac{p}{4}\cos(\varphi_n - \phi)$. We define three statistical quantities $(z_0, z_1, z_2) \equiv \left(\sum_n s_n, \frac{1}{2}\sum_n s_n \cos\varphi_n, \frac{1}{2}\sum_n s_n \sin\varphi_n\right)$, where z_0 is a measure

of the overall receptor activity and where z_1 and z_2 measure the asymmetry in the receptor states. Using the transformation $(\alpha_1, \alpha_2) \equiv (p\cos\phi, p\sin\phi)$, we can write the system's Hamiltonian as

$$\mathcal{H}_N\{s_n\} = -\sum_n \varepsilon_n s_n = -\alpha_0 z_0 - \frac{1}{2}(\alpha_1 z_1 + \alpha_2 z_2) \tag{2.3}$$

and compute its logarithm partition function as follows,

$$\begin{aligned} \ln \mathcal{Q}_N &= \ln \prod_{n=1}^{N} (e^{\varepsilon_n} + e^{-\varepsilon_n}) = \sum_{n=1}^{N} \ln[2\cosh(\alpha_0 + h_n)] \\ &= N\ln(2\cosh\alpha_0) + \frac{Np^2}{64\cosh^2\alpha_0} + \mathcal{O}(p^4), \end{aligned} \tag{2.4}$$

where in the last step the summand is expanded in powers of p and the sum is replaced by an integral over $[0, 2\pi]$.

The partition function contains all the thermodynamic information we need to infer the gradient parameters p and ϕ, or alternatively, the transformed parameters α_1 and α_2. Since $p^2 = \alpha_1^2 + \alpha_2^2$, we have by Eq. (2.4):

$$\mathrm{E}[z_{1,2}] = 2\frac{\partial \ln \mathcal{Q}_N}{\partial \alpha_{1,2}} = \frac{\alpha_{1,2} N C_0 K_d}{4(C_0 + K_d)^2} + \mathcal{O}(p^3), \tag{2.5}$$

$$\mathrm{Var}[z_{1,2}^2] = 4\frac{\partial^2 \ln \mathcal{Q}_N}{\partial \alpha_{1,2}^2} = \frac{N C_0 K_d}{2(C_0 + K_d)^2} + \mathcal{O}(p^2). \tag{2.6}$$

In addition, one can check that $\mathrm{Cov}[z_1, z_2] \approx 0$. Thus, for small p, the joint probability density of z_1 and z_2 is

$$f(z_{1,2}|\alpha_{1,2}) \approx \frac{1}{2\pi\sigma^2} \exp\left[-\frac{(z_1 - \mu\alpha_1)^2 + (z_2 - \mu\alpha_2)^2}{2\sigma^2}\right],$$

with $\mu \equiv NC_0K_d/(4(C_0 + K_d)^2)$ and $\sigma^2 = 2\mu$ [21]. It is easy to show that the *maximum likelihood estimator* (MLE) of $\alpha_{1,2}$ is $\widehat{\alpha}_{1,2} = z_{1,2}/\mu$; see also Ref. [22]. As an orthogonal transformation, the MLE of p and ϕ are given by

$$\widehat{p} = \sqrt{\widehat{\alpha}_1^2 + \widehat{\alpha}_1^2} = \mu^{-1}\sqrt{z_1^2 + z_2^2}, \tag{2.7}$$

$$\widehat{\phi} = \arctan\left(\frac{\widehat{\alpha}_2}{\widehat{\alpha}_1}\right) = \arctan\left(\frac{z_2}{z_1}\right), \tag{2.8}$$

respectively. By the properties of MLE, both $\widehat{p}$ and $\widehat{\phi}$ tend to be unbiased and normal in the large N limit, i.e., $\widehat{p} \xrightarrow{d} \mathcal{N}(p, \sigma_p^2)$ and $\widehat{\phi} \xrightarrow{d} \mathcal{N}(\phi, \sigma_\phi^2)$, where "$\xrightarrow{d}$"

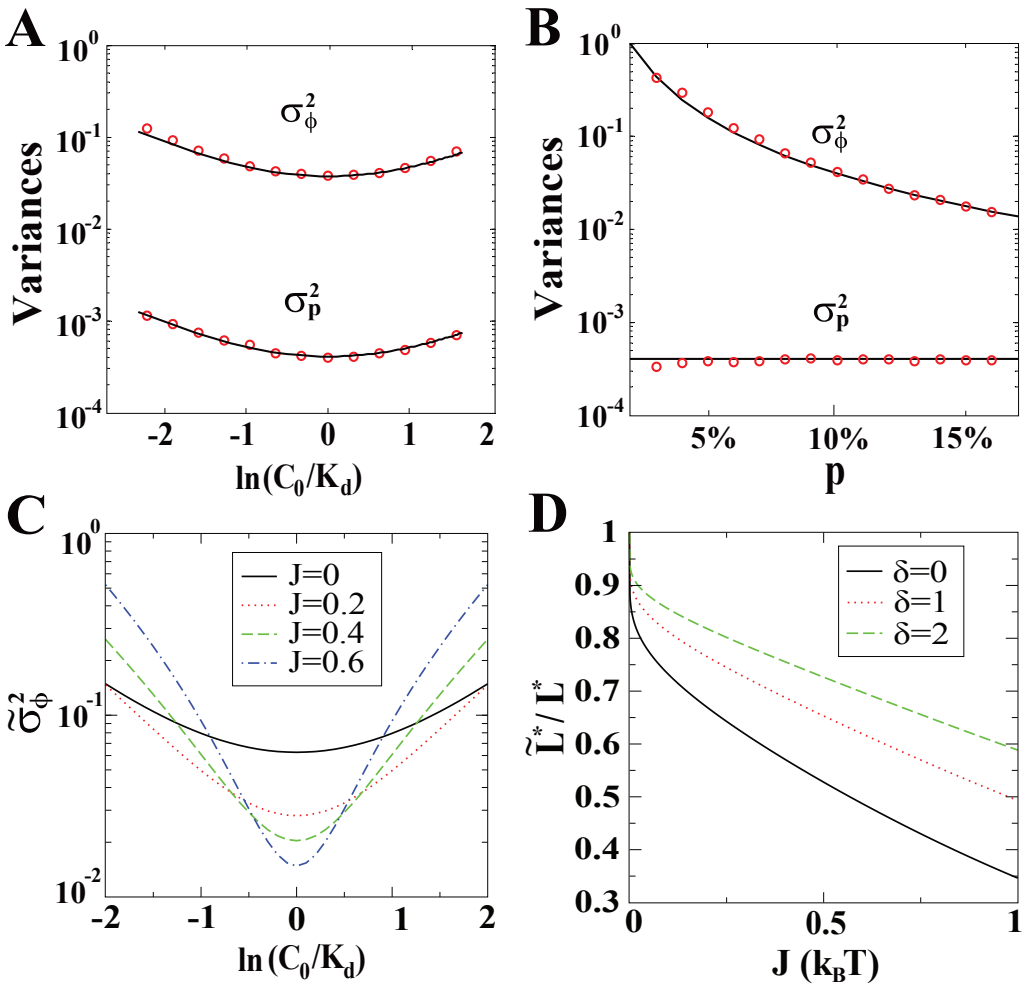


Figure 2.2: Analytical and simulation results for gradient sensing limits. (A) The uncertainties σ_p^2 and σ_ϕ^2 versus $\ln(C_0/K_d)$ under a gradient of steepness $p = 10\%$; (B) σ_p^2 and σ_ϕ^2 versus p for fixed background concentrations $C_0 = K_d$. In both A and B, the solid lines represent our analytical expressions while the symbols correspond to the sample variances of $\widehat{p}$ and $\widehat{\phi}$ computed based on 5000 independent Monte-Carlo realizations of 80000 receptors. (C) $\widetilde{\sigma}_\phi^2$ as a function of $\ln(C_0/K_d)$ for different values of the cooperativity strength J, under a gradient of steepness $p = 8\%$ and using $N = 80000$. (D) The critical cell size below which spatial gradient sensing is ineffective, normalized by the critical cell size in the absence of cooperativity, as a function of J.

denotes convergence in distribution. The asymptotic variances σ_p^2 and σ_ϕ^2 can be derived from the Fisher information matrix [22], which is diagonal here since p and ϕ are independent. Thus, we have

$$\sigma_p^2 = 1/\mathrm{E}\left[(\partial_p \ln f)^2\right] = \frac{\sigma^2}{\mu^2} = \frac{2}{\mu} = \frac{8(C_0+K_d)^2}{NK_dC_0}, \tag{2.9}$$

$$\sigma_\phi^2 = 1/\mathrm{E}\left[(\partial_\phi \ln f)^2\right] = \frac{\sigma^2}{\mu^2 p^2} = \frac{2}{\mu p^2} = \frac{\sigma_p^2}{p^2}. \tag{2.10}$$

According to the Cramér-Rao inequality, σ_p^2 and σ_ϕ^2 set the lowest uncertainties of gradient measurements from an instantaneous sampling of the receptor states [22]. The analytical approximation of each variance is plotted as a function of the background concentration C_0 (Fig. 2.2A) and the gradient steepness p (Fig. 2.2B), which agrees well with the sample variance of $\widehat{p}$ or $\widehat{\phi}$ numerically obtained from our Monte-Carlo simulations. We can see that both σ_p^2 and σ_ϕ^2 reach a minimum at $C_0 = K_d$ (Fig. 2.2A), while only the error in direction estimation depends on the gradient steepness (i.e., $\sigma_\phi^2 \sim p^{-2}$) as shown in Fig. 2.2B. Since the gradient steepness increases with the cell size (i.e., $p \sim L$), larger cells are able to sense the gradient direction with higher accuracy.

The above results are derived from a single snapshot of the system. If the cell integrates receptor signals over some time interval $\mathcal{T}$, then averaging over multiple measurements can appreciably reduce the errors of gradient sensing. However, the capacity of such averaging is limited by the expected time it takes for every independent measurement. As shown in [6, 12], the time to complete a single measurement is roughly twice the system's correlation time τ, resulting from the diffusion and binding of ligands. So the number of independent measurements that a cell can make within $\mathcal{T}$ is roughly $\mathcal{T}/(2\tau)$, which leads to a corresponding reduction of measurement uncertainties. The correlation time can be decomposed as $\tau = \tau_{\mathrm{rec}} + \tau_{\mathrm{diff}}$, where $\tau_{\mathrm{rec}} = 1/(k_- + C_0 k_+)$ is the timescale of receptor-ligand reaction and τ_{diff} describes the diffusive transport time of ligands. Let $\eta \equiv \tau_{\mathrm{diff}}/\tau_{\mathrm{rec}}$, then the measurement is reaction-limited if $\eta \ll 1$ and diffusion-limited if $\eta \gg 1$ [23]. From the above arguments we find that averaging signals over $\mathcal{T}$ yields a

lower uncertainty of the gradient estimate,

$$\sigma_{p,\mathcal{T}}^2 \simeq \frac{2\tau}{\mathcal{T}}\sigma_p^2 = \frac{4\tau_{rec}(1+\eta)}{\mu\mathcal{T}} = \frac{16(1+\eta)}{N\mathcal{T}k_-}\left(1+\frac{K_d}{C_0}\right). \tag{2.11}$$

For small background concentrations ($C_0 \ll K_d$), $\tau_{\text{diff}} = N/(2\pi LDK_d)$ where D denotes the ligand diffusion coefficient [10, 12, 23], and the uncertainty reduces to

$$\sigma_{p,\mathcal{T}}^2 \simeq \frac{16}{N\mathcal{T}C_0k_+} + \frac{8}{\pi\mathcal{T}DLC_0}. \tag{2.12}$$

This expression resembles the result derived for the one-dimensional case [17] and contains two terms: the first one is determined by the chemical kinetics, and the second one, up to a geometric constant, is exactly the Berg-Purcell limit [10, 14]. We shall have similar results for the direction inference, since $\sigma_{\phi,\mathcal{T}}^2 = \sigma_{p,\mathcal{T}}^2/p^2$. For typical eukaryotic cells, it has been estimated [12, 23] that $\eta \ll 1$, which implies

$$\sigma_{\phi,\mathcal{T}}^2 \simeq \frac{16(1+K_d/C_0)}{Np^2\mathcal{T}k_-} \sim \frac{1}{Np^2}. \tag{2.13}$$

We can relate the uncertainty in the direction measurement to the cell size L. Assuming that the number of receptors in our model scales with the cell size as $N = N_0L^\delta$ with $0 \le \delta \le 2$, we find $\sigma_{\phi,\mathcal{T}}^2 \sim L^{-(2+\delta)}$. For comparison, the Berg-Purcell analysis considered only the mean concentration measurement, with a limit that scale as $\sigma_{c,\mathcal{T}}^2 \sim L^{-1}$ [10]. Our results thus indicate that directional sensing is much more sensitive to the cell size.

Our analysis above, which extends beyond the Berg-Purcell framework by providing a direct calculation of the directional sensing limit $\sigma_{\phi,\mathcal{T}}^2$, was carried out for independent (i.e. non-cooperative) receptors, as is assumed to be the case for most eukaryotic cells that have been studied. It has been proposed that cooperativity can dampen the fluctuations in receptor signals and thus help concentration sensing to approach the physical limit of diffusive counting noise [13]. For spatial gradient sensing, we now ask about possible effects of receptor cooperativity as has been found in many bacterial cells [24, 25, 26, 27, 28]. Intuitively, short-range interactions make it possible for receptors to collectively respond and sharpen the asymmetry of receptor signals. It is natural to speculate that such enhanced sensitivity may set new and lower limits for directional sensing. To incorporate potential

receptor cooperativity, we extend our model to include a nearest-neighbor interaction J (again, in units of k_BT). Now, the activity of a receptor, still represented by s_n, is determined not only by the local concentration but also by the states of its neighboring receptors. This means that an unbound receptor is not necessarily inactive, as it may have been affected by active receptors nearby.

Because the local concentration is identical for nearest-neighbor sites (i.e., $\varepsilon_n = \varepsilon_{n\pm1}$), the Hamiltonian of our Ising chain can be written in a symmetric form:

$$\widetilde{\mathcal{H}}_N\{s_n\} = -\sum_{n=1}^{N}\left[Js_ns_{n+1} + \frac{\varepsilon_n(s_n + s_{n+1})}{2}\right], \tag{2.14}$$

with the boundary condition $s_{N+1} = s_1$. The corresponding partition function is $\widetilde{\mathcal{Q}}_N = \sum_{s_1}...\sum_{s_N} e^{-(H_0+H_1)}$, where $H_0 \equiv -\sum_n[Js_ns_{n+1} + \alpha_0(s_n + s_{n+1})/2]$ represents the Hamiltonian of an isotropic reference system and where $H_1 \equiv -\sum_n s_nh_n = -\frac{p}{4}\sum_n s_n\cos(\varphi_n - \phi)$ results from the spatial heterogeneity in concentration. For small p, one can view H_1 as a perturbation to H_0. The partition function of the reference system, $\widetilde{\mathcal{Q}}_N^{(0)} = \sum_{s_1}...\sum_{s_N} e^{-H_0}$, is well-known and exactly solvable by the transfer matrix method: $\widetilde{\mathcal{Q}}_N^{(0)} = \lambda_+^N + \lambda_-^N$, with

$$\lambda_\pm = e^J\cosh\alpha_0 \pm \sqrt{e^{-2J} + e^{2J}\sinh^2\alpha_0}. \tag{2.15}$$

More technical details are left in the next section. So we have $\ln\widetilde{\mathcal{Q}}_N^{(0)} \simeq N\ln\lambda_+$. The statistical perturbation theory inspires us to write

$$\begin{aligned}\widetilde{\mathcal{Q}}_N &= \widetilde{\mathcal{Q}}_N^{(0)}\sum_{s_1}...\sum_{s_N} e^{-H_0}\frac{e^{-H_1}}{\widetilde{\mathcal{Q}}_N^{(0)}} = \widetilde{\mathcal{Q}}_N^{(0)}\langle e^{-H_1}\rangle \\ &\simeq \lambda_+^N\left[1 + \frac{p}{4}\sum_n\langle s_n\rangle\cos\theta_n + \frac{p^2}{32}\sum_{n,m}\langle s_ns_m\rangle\cos\theta_n\cos\theta_m\right],\end{aligned} \tag{2.16}$$

where we denote $\theta_n \equiv \varphi_n - \phi$ for short and use $\langle\cdot\rangle$ to represent the expectation over the reference system. Due to isotropy, $\langle s_n\rangle$ is independent of its location (index n) and hence $\sum_n\langle s_n\rangle\cos\theta_n = \langle s_n\rangle\sum_n\cos\theta_n = 0$. With details given in the next section, we further calculate that

$$\sum_{n,m}\langle s_ns_m\rangle\cos\theta_n\cos\theta_m = \frac{N}{2}\cdot\frac{1+2\xi}{1+e^{4J}\sinh^2\alpha_0}, \tag{2.17}$$

where $\xi \equiv [\ln(\lambda_+/\lambda_-)]^{-1}$ defines the correlation length of the classic Ising chain [29]. Finally, the log-partition function of our model is found to be

$$\ln \widetilde{\mathcal{Q}}_N \simeq N \ln \lambda_+ + \frac{Np^2(1+2\xi)}{64(1+e^{4J}\sinh^2\alpha_0)} + \mathcal{O}(p^3), \tag{2.18}$$

which reduces to Eq. (2.4) as $J \to 0$.

Now we rewrite $\widetilde{\mathcal{H}}_N = -J\sum_n s_n s_{n+1} - \alpha_0 z_0 - (\alpha_1 z_1 + \alpha_2 z_2)/2$, with the same notations for α_i and z_i, $i = 0, 1, 2$. As has been demonstrated before, the MLE of α_1 and α_2 can be found from the joint Gaussian distribution of z_1 and z_2, except now we have to replace μ by

$$\widetilde{\mu} \equiv \frac{N(1+2\xi)}{16(1+e^{4J}\sinh^2\alpha_0)}. \tag{2.19}$$

So the MLE of p and ϕ are given by

$$\widetilde{p} = \widetilde{\mu}^{-1}\sqrt{z_1^2+z_2^2} \xrightarrow{d} \mathcal{N}(p, \widetilde{\sigma}_p^2) \tag{2.20}$$

$$\widetilde{\phi} = \arctan(z_2/z_1) \xrightarrow{d} \mathcal{N}(\phi, \widetilde{\sigma}_\phi^2). \tag{2.21}$$

Similar to Eqs. (2.9) and (2.10), their variances are $\widetilde{\sigma}_p^2 = 2/\widetilde{\mu}$ and $\widetilde{\sigma}_\phi^2 = \widetilde{\sigma}_p^2/p^2 = 2/(\widetilde{\mu}p^2)$. As long as we are not near any phase transition point, the expected single measurement time will remain dominated by the processes of diffusion and binding/unbinding of ligand molecules [13]. Thus, averaging signals over $\mathcal{T}$ will give $\widetilde{\sigma}_{p,\mathcal{T}}^2 \simeq 4\tau_{\rm rec}(1+\eta)/(\widetilde{\mu}\mathcal{T})$ and $\widetilde{\sigma}_{\phi,\mathcal{T}}^2 = \widetilde{\sigma}_{p,\mathcal{T}}^2/p^2$. We plot $\widetilde{\sigma}_\phi^2$ as a function of $\ln(C_0/K_d)$ for different values of J in Fig. 2.2C. Regardless of the receptor coupling strength, this error is minimal at $C_0 = K_d$ (or $\alpha_0 = 0$) where the correlation length becomes $\xi = 1/\ln(\coth J) \simeq \frac{1}{2}e^{2J}$ and

$$\widetilde{\sigma}_\phi^2 \simeq \frac{32}{Np^2(1+e^{2J})} = \frac{\sigma_\phi^2}{1+e^{2J}}. \tag{2.22}$$

2.3 Discussion

Receptor cooperativity may help a smaller cell of diameter $\widetilde{L}$ to reach the same level of directional sensing accuracy as achieved by a larger cell with diameter L but non-cooperative receptors, i.e., $\widetilde{\sigma}_\phi^2(\widetilde{L}) = \sigma_\phi^2(L)$. By our previous scaling

assumption, the receptor number of the smaller cell is $\widetilde{N} = N(\widetilde{L}/L)^{\delta}$. If L^* denotes a critical cell length below which spatial sensing is infeasible with independent receptors, then adding cooperativity will result in a smaller critical size, given by $\widetilde{L}^* \simeq L^*(1+e^{2J})^{-1/(2+\delta)}$ at $C_0 = K_d$. This is shown in Fig. 2.2D where we have plotted $\widetilde{L}^*/L^*$ as a function of J for three different values of the scaling factor δ. As a specific example, we take $L^* = 8\ \mu m$ which corresponds to the typical size of a *Dictyostelium* amoeba. Then, for a coupling strength $J = 0.5$, the new critical cell length becomes $\widetilde{L}^* \sim$ 4-6 μm, comparable to the size of many bacterial cells. It is worth remarking that although receptor interaction improves the precision of gradient sensing for C_0 close to K_d, it enlarges the errors when C_0 is far away from K_d (Fig. 2.2C). Note that the receptor configuration tends to be homogeneous in both the large and small concentration extremes, i.e., it is dominated either by active receptors at $C_0 \gg K_d$ or by inactive receptors at $C_0 \ll K_d$. Cooperativity exaggerates such a tendency to reach an ordered phase, an effect which interferes with the cell's ability to extract information about the spatial heterogeneity from receptor states. Therefore, the improved accuracy at C_0 near K_d is accompanied by a narrowed range of background concentrations for which the cell can be sufficiently sensitive (Fig. 2.2C). Such a tradeoff could be a limiting factor for the introduction of receptor coupling into the spatial sensing mechanism.

It is commonly believed that prokaryotic cells such as *E. coli* are too small to perform spatial measurements of chemical gradients. However, recent experimental observations show that at least one type of vibrioid bacteria (typical size 2×6 μm) are able to spatially sense gradients along distances as short as 5 μm, and the proposed sensing system has two bipolar sensor regions containing receptor clusters [20]. Our calculations allow for the possibility that smaller organisms could employ the spatial sensing strategy with the aid of short-range receptor interactions. As spatial sensing is argued to be superior to temporal sensing for fast swimming bacteria [20, 30], this possibility is of significant theoretical interest and remains a challenge for future empirical studies.

2.4 Technical Details

By introducing the nearest-neighbor interaction J, the original spin system becomes a finite closed Ising chain. As mentioned in the main text, since the local concentration is virtually identical for nearest-neighbor sites (i.e., $C_{n\pm1} = C_n$ and consequently $\varepsilon_{n\pm1} = \varepsilon_n$), the Hamiltonian of our Ising model can be written in the following symmetric form:

$$\widetilde{\mathcal{H}}_N\{s_n\} = -\sum_{n=1}^{N}\left[Js_ns_{n+1} + \frac{\varepsilon_n}{2}(s_n + s_{n+1})\right], \tag{2.23}$$

with the boundary condition $s_{N+1} = s_1$. As $\varepsilon_n \equiv \alpha_0 + h_n$, the partition function of our Ising model is

$$\widetilde{\mathcal{Q}}_N = \sum_{s_1=\pm1} ... \sum_{s_N=\pm1} e^{-\widetilde{\mathcal{H}}_N} = \sum_{s_1=\pm1} ... \sum_{s_N=\pm1} e^{-(H_0+H_1)}, \tag{2.24}$$

where

$$H_0 \equiv -\sum_{n=1}^{N}\left[Js_ns_{n+1} + \frac{\alpha_0}{2}(s_n + s_{n+1})\right] \tag{2.25}$$

represents the Hamiltonian of an isotropic reference system and where

$$H_1 \equiv -\sum_{n=1}^{N} s_nh_n = -\frac{p}{4}\sum_{n=1}^{N} s_n\cos(\varphi_n - \phi) \tag{2.26}$$

results from the spatial heterogeneity in concentrations. For small p (shallow gradients), we can view H_1 as a perturbation term to H_0. The partition function of the isotropic reference system, $\widetilde{\mathcal{Q}}_N^{(0)}$, is actually identical to that of the classic Ising chain, which can be exactly solved by introducing the transfer matrix [29]:

$$\mathcal{P} \equiv \begin{pmatrix} e^{J+\alpha_0} & e^{-J} \\ e^{-J} & e^{J-\alpha_0} \end{pmatrix} \tag{2.27}$$

such that

$$\langle s_n|\mathcal{P}|s_{n+1}\rangle = \exp\left[Js_ns_{n+1} + \frac{\alpha_0}{2}(s_n + s_{n+1})\right], \tag{2.28}$$

and

$$\begin{aligned}\widetilde{\mathcal{Q}}_N^{(0)} &= \sum_{s_1}...\sum_{s_N} e^{-H_0} = \sum_{s_1}...\sum_{s_N} \exp\left\{\sum_n [Js_ns_{n+1} + \alpha_0(s_n + s_{n+1})/2]\right\} \\ &= \sum_{s_1}...\sum_{s_N} \langle s_1|\mathcal{P}|s_2\rangle\langle s_2|\mathcal{P}|s_3\rangle...\langle s_{N-1}|\mathcal{P}|s_N\rangle\langle s_N|\mathcal{P}|s_1\rangle \\ &= \sum_{s_1}\langle s_1|\mathcal{P}^N|s_1\rangle = \mathrm{Trace}(\mathcal{P}^N) = \lambda_+^N + \lambda_-^N, \end{aligned} \tag{2.29}$$

where $\lambda_\pm = e^J \cosh\alpha_0 \pm \sqrt{e^{-2J} + e^{2J}\sinh^2\alpha_0}$ are the eigenvalues of the transfer matrix $\mathcal{P}$. Since $\lambda_+ > \lambda_-$, we have $\ln \widetilde{\mathcal{Q}}_N^{(0)} \to N \ln\lambda_+$ for large N.

We can then apply statistical perturbation theory, which yields

$$\begin{aligned}\widetilde{\mathcal{Q}}_N &= \widetilde{\mathcal{Q}}_N^{(0)} \sum_{s_1}...\sum_{s_N} e^{-H_1}\frac{e^{-H_0}}{\widetilde{\mathcal{Q}}_N^{(0)}} = \widetilde{\mathcal{Q}}_N^{(0)}\langle e^{-H_1}\rangle \\ &\simeq \lambda_+^N\left[1 + \frac{p}{4}\sum_n \langle s_n\rangle\cos\theta_n + \frac{p^2}{32}\sum_{n,m}\langle s_ns_m\rangle\cos\theta_n\cos\theta_m\right]. \end{aligned} \tag{2.30}$$

Here, we denote $\theta_n \equiv \varphi_n - \phi$ and use $\langle\cdot\rangle$ to represent the expectation over the reference system. As mentioned in the main text, $\sum_n\langle s_n\rangle\cos\theta_n = 0$ due to isotropy. For the classic Ising chain (i.e., the reference system), the spin-spin correlation is given by $\langle s_ns_m\rangle = \cos^2 2\omega + \gamma^{|n-m|}\sin^2 2\omega$, where $\gamma \equiv \lambda_-/\lambda_+$ and the parameter ω is defined by the equation $\cot 2\omega = e^{2J}\sinh\alpha_0$ for $0 < \omega < \pi/2$ [29]. Since

$$\sum_n\sum_m \cos^2 2\omega\cos\theta_n\cos\theta_m = \cos^2 2\omega\sum_n\cos\theta_n\sum_m\cos\theta_m = 0, \tag{2.31}$$

we only have to calculate $\sum_n\sum_m\cos\theta_n\cos\theta_m\gamma^{|n-m|}$ which can be expanded into two parts:

$$\begin{aligned}\sum_n\sum_m\cos\theta_n\cos\theta_m\gamma^{|n-m|} &= \sum_n\cos\theta_n\sum_m\cos[(\theta_m-\theta_n)+\theta_n]\gamma^{|n-m|} \\ &= \sum_n\cos^2\theta_n\sum_m\cos(\theta_m-\theta_n)\gamma^{|n-m|} \\ &- \sum_n\cos\theta_n\sin\theta_n\sum_m\sin(\theta_m-\theta_n)\gamma^{|n-m|}. \end{aligned} \tag{2.32}$$

The second term of Eq. (2.32) vanishes since we have

$$\sum_m\sin(\theta_m-\theta_n)\gamma^{|n-m|} = \sum_{j=-N/2}^{N/2}\sin(2\pi j/N)\gamma^{|j|} = 0, \tag{2.33}$$

while its first term is identical to

$$\sum_n \cos^2\theta_n \sum_{j=-N/2}^{N/2} \cos(2\pi j/N)\gamma^{|j|} = \sum_n \cos^2\theta_n \left[1 + 2\sum_{j=1}^{N/2} \cos(2\pi j/N)\gamma^j\right]. \quad (2.34)$$

In the large N limit, we have that $\sum_n \cos^2\theta_n \simeq N/2$, and if we let $x \equiv 2\pi j/N$, then

$$\begin{aligned} \sum_{j=1}^{N/2} \cos\left(\frac{2\pi j}{N}\right)\gamma^j \quad &\simeq \quad \frac{N}{2\pi}\int_0^\pi \cos(x)\exp\left(\frac{xN}{2\pi}\ln\gamma\right)dx \\ &\xrightarrow{N\to\infty} \quad \frac{-1}{\ln\gamma} = \left[\ln\left(\frac{\lambda_+}{\lambda_-}\right)\right]^{-1} \equiv \xi, \end{aligned} \quad (2.35)$$

where ξ defines the correlation length of the classic Ising chain [29]. Combining Eqs. (2.32-2.35), we can derive that

$$\begin{aligned} \sum_n \sum_m \langle s_n s_m\rangle \cos\theta_n \cos\theta_m &= \frac{N(1+2\xi)}{2}\sin^2 2\omega \\ &= \frac{N}{2}\frac{1+2\xi}{\cot^2 2\omega + 1} \\ &= \frac{N}{2}\frac{1+2\xi}{1 + e^{4J}\sinh^2\alpha_0}. \end{aligned} \quad (2.36)$$

By Eq. (2.30) and Eq. (2.36), we find the following log-partition function of our Ising model in the small p limit:

$$\ln\widetilde{\mathcal{Q}}_N \simeq N\ln\lambda_+ + \frac{Np^2(1+2\xi)}{64(1+e^{4J}\sinh^2\alpha_0)} + \mathcal{O}(p^3). \quad (2.37)$$

This final result is then used in the text to study the consequences of receptor interactions on gradient sensing.

2.5 Concluding Remarks

Many eukaryotic cells are able to detect chemical gradients by directly measuring spatial concentration differences. The precision of such gradient sensing is limited by fluctuations in the binding of diffusing particles to specific receptors on the cell surface. Here, we explore the physical limits of the spatial sensing mechanism by modeling the chemotactic cell as an Ising spin chain subject to a spatially

varying field. This allows us to derive the *maximum likelihood estimators* of the gradient parameters as well as explicit expressions for their asymptotic uncertainties. Our analytical results demonstrate that the accuracy to sense the gradient direction increases dramatically with the cell size. Also, we show that this accuracy can be improved significantly by introducing neighboring receptor cooperativity. Thus, receptor coupling may open the possibility for small bacteria to perform spatial measurements of gradients, as supported by a recent experimental finding.

2.6 Acknowledgements

Chapter 2, in part, is the published material as it appears in Physical Review Letters, (2010), Hu, Bo; Chen, Wen; Rappel, Wouter-Jan; Levine, Herbert. The dissertation author was the primary investigator and author of this paper.

Bibliography

[1] C.A. Parent and P.N. Devreotes, Science. **284**, 765 (1999).

[2] R.M. Macnab and D.E. Koshland, Proc. Natl. Acad. Sci. U.S.A. **69**, 2509 (1972).

[3] V. Sourjik and H.C. Berg, Proc. Natl. Acad. Sci. U.S.A. **99**, 123 (2002).

[4] P.J.V. Haastert and P.N. Devreotes, Nat. Rev. Mol. Cell Biol. **5**, 626 (2004).

[5] L. Song, S.M. Nadkarni, H.U. Bödeker, C. Beta, A. Bae, C. Franck, W.-J. Rappel, W.F. Loomis, and E. Bodenschatz, Eur. J. Cell Biol. **85**, 981 (2006).

[6] P.J.V. Haastert and M. Postma, Biophys. J. **93**, 1787 (2007).

[7] D. Fuller, W. Chen, M. Adler, A. Groisman, H. Levine, W.J. Rappel, W.F. Loomis, Proc. Natl. Acad. Sci. U.S.A. **107**, 9656 (2010).

[8] M. Ueda, Y. Sako, T. Tanaka, P.N. Devreotes, and T. Yanagida, Science, **294**, 864 (2001).

[9] M. Ueda and T. Shibata, Biophys. J. **93**, 11 (2007).

[10] H.C. Berg and E.M. Purcell, Biophys. J. **20**, 193 (1977).

[11] W. Bialek and S. Setayeshgar, Proc. Natl. Acad. Sci. U.S.A. **102**, 10040 (2005).

[12] K. Wang, W.-J. Rappel, R. Kerr, and H. Levine, Phys. Rev. E **75**, 061905 (2007).

[13] W. Bialek and S. Setayeshgar, Phys. Rev. Lett. **100**, 258101 (2008).

[14] R.G. Endres and N.S. Wingreen, Proc. Natl. Acad. Sci. U.S.A. **105**, 15749 (2008).

[15] R.G. Endres and N.S. Wingreen, Phys. Rev. Lett. **103**, 158101 (2009).

[16] G. Aquino and R.G. Endres, Phys. Rev. E **81**, 021909 (2010).

[17] R.G. Endres and N.S. Wingreen, Prog. Biophys. Mol. Biol. **100**, 33 (2009).

[18] W.-J. Rappel and H. Levine, Phys. Rev. Lett. **100**, 228101 (2008).

[19] W.-J. Rappel and H. Levine, Proc. Natl. Acad. Sci. U.S.A. **105**, 19270 (2008).

[20] R. Thar and M. Kühl, Proc. Natl. Acad. Sci. U.S.A. **100**, 5748 (2003).

[21] B. Hu, D. Fuller, W.F. Loomis, H. Levine, and W.-J. Rappel, Phys. Rev. E **81**, 031906 (2010).

[22] S.M. Kay, *Fundamentals of Statistical Signal Processing: Estimation Theory* (Prentice Hall PTR, Upper Saddle River, NJ, 1993), Vol. 1, Chap. 3.

[23] D.A. Lauffenburger and J.J. Linderman, *Receptors: Models for Binding, Trafficking, and Signaling* (Oxford University Press, New York, 1993).

[24] Y. Shi and T. Duke, Phys. Rev. E **58**, 6399 (1998).

[25] B.A. Mello and Y. Tu, Proc. Natl. Acad. Sci. U.S.A. **100**, 8223 (2003).

[26] B.A. Mello and Y. Tu, Proc. Natl. Acad. Sci. U.S.A. **102**, 17354 (2005).

[27] J.E. Keymer, R.G. Endres, M. Skoge, Y. Meir, and N.S. Wingreen, Proc. Natl. Acad. Sci. U.S.A. **103**, 1786 (2006).

[28] M.L. Skoge, R.G. Endres, and N.S. Wingreen, Biophys. J. **90**, 4317 (2006).

[29] R.J. Baxter, *Exactly Solved Models in Statistical Mechanics* (Academic, London, 1982), Chap. 2.

[30] D.B. Dusenbery, Biophys. J. **74**, 2272 (1998).

Chapter 3

Stochastic Modeling of Eukaryotic Chemotaxis

3.1 Introduction

During chemotaxis, cells direct their movement by sensing chemical gradients. Chemotaxis plays an important role in various biological processes including fertilization, neuronal development, wound healing and cancer metastasis [1, 2]. Unlike prokaryotes, eukaryotic cells use a spatial measurement of the asymmetric distribution of bound receptors following the external gradient. These bound receptors trigger the activation of intracellular signaling pathways, eventually leading to the generation of directional movement. Interestingly, eukaryotic cells are able to direct their motion in shallow gradients. For example, the social amoeba *Dictyostelium discoideum* is observed to crawl up a chemoattractant gradient when the front-back difference in the concentration is around 1% [3, 4]. Furthermore, the cells respond even when the average local concentration is well below the dissociation constant K_d. These findings has led to significant interest from the biophysics community in understanding the effect of noise on chemotaxis [5, 6, 7, 8, 9, 10, 11, 12].

Studies to date have mainly focused on fluctuations in gradient sensing, arising for example from stochastic receptor dynamics [6, 10]. However, there are other

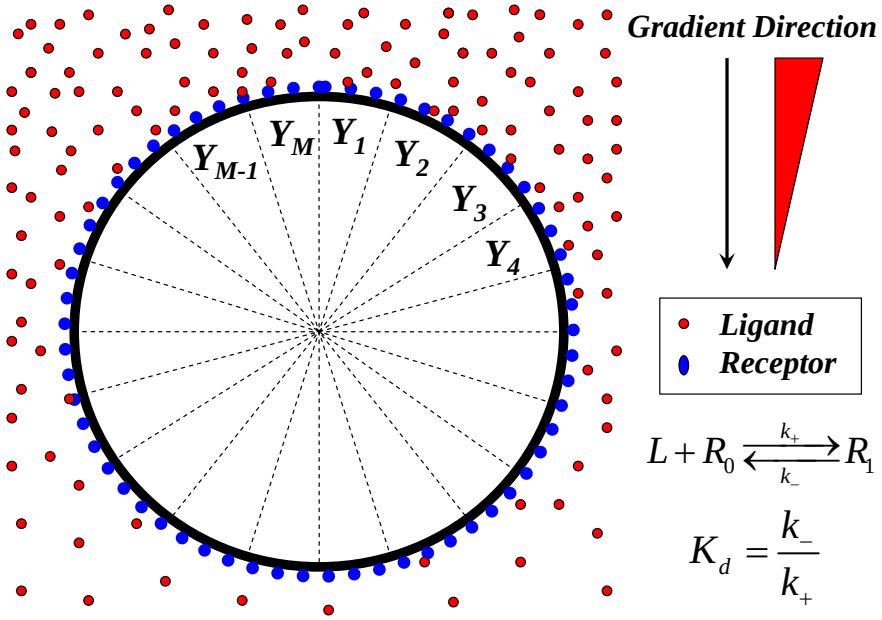


Figure 3.1: Schematic representation of our model. The forward rate k_+ and backward rate k_- determine the transition between the unoccupied R_0 and occupied R_1 states. The dissociation constant K_d is the ligand concentration at which half the receptors are bound in equilibrium.

sources of noise, as is evidenced by the fact that cells move *randomly* in the absence of directional information [13, 14]. The simplest approach to adding random motility to directional bias is to assume that the cell executes Brownian motion in a deterministic periodic potential [15]; however this approach fails to take into account uncertainties in evaluating gradient steepness and direction. Thus, what is needed is a new model of directed cell motility that takes into account both sources of fluctuations. Such a model should be able to relate the relative importance of gradient-determination noise versus motility noise to testable predictions for the behavior of chemotactic cells. Here, we propose a phenomenological, stochastic differential equation (SDE) model for this purpose and compare its predictions with the available data. As we will see, our approach naturally accounts for the unusual shape of the directional probability distribution for chemotaxing cells.

3.2 Model

In our model, the cellular surface takes a circular geometry where N independent receptors are uniformly distributed (Fig. 3.1). We divide the surface into M sectors such that the local ligand concentration near each sector is constant while the number of receptors in each sector $N_m = N/M$ is large enough for the continuous approximation. For *Dictyostelium*, a typical value is $N = 60000$, and one may choose $M = 300$ and $N_m = 200$. We define the gradient steepness parameter as $p = \frac{L}{C_0}\frac{dC}{dr}$, where C_0 is the average local ligand concentration across the cell length L. Then, the local concentration at the m_{th} sector with angular position φ_m is given by

$$C_m = C_0[1 + \frac{p}{2}\cos(\varphi_m - \phi)], \tag{3.1}$$

where ϕ specifies the gradient direction. The time for receptor decorrelation is dominated by the individual receptor rate $\tau_m = (k_- + k_+ C_m)^{-1}$ which is typically faster than the process by which motion can be mechanically altered. Here we have used the fact that under typical conditions the contribution of ligand diffusion to the receptor correlation can be ignored [6, 7]. This allows us to use the white-noise approximation [7, 16] in which the number of occupied receptors is

$$Y_m = \langle Y_m \rangle + \eta_m = \frac{N_m C_m}{C_m + K_d} + \eta_m, \tag{3.2}$$

for $m = 1, ..., M$, with

$$\langle \eta_m(t)\eta_n(s) \rangle \approx \frac{N_m C_m K_d}{(C_m + K_d)^2}\delta(t - s)\delta_{mn}. \tag{3.3}$$

Thus, the receptor signal is decomposed into M independent Gaussian random variables.

The simplest estimate a cell can make of the gradient is obtained by the following statistic:

$$Z = \sum_{m=1}^{M} Y_m \cos\varphi_m + i\sum_{m=1}^{M} Y_m \sin\varphi_m \equiv z_1 + iz_2. \tag{3.4}$$

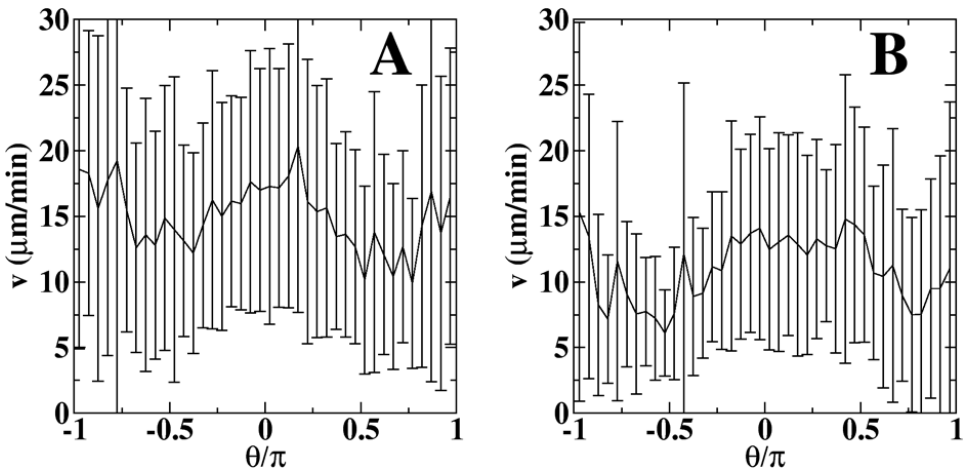


Figure 3.2: The average cell speed in the experiments of Ref. [4] as a function of angle for p=5% (A) and p=10% (B). For each gradient steepness, the speed was computed by tracking the position of the centroid of 30-40 cells during 8 minutes. For more experimental details, see Ref. [4].

When M is large, one can evaluate Z via replacing the sum by an integral. For small gradients ($p < 10\%$), the integrand can be expanded around p and we find

$$\langle Z \rangle \approx \frac{pNC_0K_de^{i\phi}}{4(C_0+K_d)^2} + \mathcal{O}(p^3) \equiv \nu e^{i\phi} + \mathcal{O}(p^3), \tag{3.5}$$

$$\langle z_{1,2}^2 \rangle - \langle z_{1,2} \rangle^2 \approx \frac{NC_0K_d}{2(C_0+K_d)^2} + \mathcal{O}(p^2) \equiv \sigma^2 + \mathcal{O}(p^2). \tag{3.6}$$

It is easy to check that z_1 and z_2 are uncorrelated Gaussian random variables, with different means but the same variance. This implies that Z is a complex Gaussian variable which can be written in polar coordinates as $Z = \rho e^{i\psi}$. Here, ρ measures the degree of asymmetry in the ligand-bound receptor distribution while the phase ψ estimates the gradient direction ϕ. Mathematically, ρ follows the Rice distribution and ψ takes a symmetric unimodal circular distribution [17]. It was found that for large signal-to-noise ratio (SNR$= \nu/\sigma \gtrsim 3$) both ρ and ψ are asymptotically Gaussian [17]. Thus, $\rho \approx \nu + \eta_\rho$ with $\langle \eta_\rho(t)\eta_\rho(s)\rangle = \sigma^2\delta(t-s)$, and $\psi \approx \phi + \eta_\psi$ with $\langle \eta_\psi(t)\eta_\psi(s)\rangle = (\sigma^2/\nu^2)\delta(t-s)$. As an orthogonal transformation from the Cartesian coordinates, η_ρ is independent of η_ψ. For typical *Dictyostelium* values we find that SNR> 3, consistent with the Gaussian approximation.

Cellular motion can be decomposed into two stochastic processes: speed and direction. Recent experimental data in *Dictyostelium* [4] show that the aver-

age speed is roughly identical for all directions. In these experiments, cells were exposed to stable exponential chemoattractant profiles using microfluidic devices. The centroid of each cell in the field of view was automatically tracked every 5s for 100 frames. Cells that moved the furthest without colliding with another cell were chosen for data analysis. Ten to twenty-five such cells were collected in each experiment, giving thousands of data points for each particular gradient. The average speed as a function of the angle is plotted in Fig. 3.2 for two different gradient steepnesses. From this figure, we can conclude that any possible correlation between angle and speed is smaller than can be obtained from the data. Thus, we restrict ourselves to the directional process, parameterized by the migration angle $\theta(t)$, by assuming a uniform migration speed.

Let us temporarily suppose that cells have perfect knowledge about the gradient direction ϕ. In general, the equation of $\theta(t)$ can be written as

$$\frac{d\theta}{dt} = G(\rho, \theta - \phi) + \eta_0, \tag{3.7}$$

along with $\langle \eta_0(t)\eta_0(s)\rangle = \sigma_0^2\delta(t-s)$. The incorporation of the gradient-independent noise η_0 above allows the cell to perform a random walk in the absence of any gradient. Note that unlike a recent study of random motility [13], we do not include colored noise in our model. The function $G(\rho, \theta)$ must exhibit the symmetry properties [15]: (1) 2π-periodicity, $G(\rho, \theta \pm 2n\pi) = G(\rho, \theta)$ for any integer n; (2) polar symmetry, $G(\rho, \theta \pm \pi) = -G(\rho, \theta)$, because the system's polarity will be reversed under the reversal of gradient direction; (3) reflection symmetry, $G(\rho, -\theta) = -G(\rho, \theta)$, i.e. cells cannot distinguish between left and right with respect to the direction ϕ. The simplest form obeying these requirements is $G(\rho, \theta - \phi) = -\beta(\rho)\sin(\theta - \phi)$. Of course, cells have only imperfect knowledge of the gradient direction. The phase variable ψ in our model serves as an unbiased estimator of ϕ for the cell. Thus, we arrive at the phenomenological Langevin equation

$$\frac{d\theta}{dt} = -\beta(\rho)\sin(\theta - \psi) + \eta_0. \tag{3.8}$$

This phenomenological equation describes a chemotactic cell trying to align its movement with the estimated gradient direction ψ. The first term describes a

gradient-dependent restoring force which steers the cell toward the gradient direction and which contains gradient-dependent fluctuations (arising from receptor-ligand dynamics and downstream pathways) while the second term represents gradient independent noise in the random motility machinery.

Without loss of generality, we will set $\phi = 0$. In the small noise limit we can perform a Taylor expansion

$$\frac{d\theta}{dt} \approx -\beta(\nu)\sin\theta + \beta'(\nu)\sin\theta\eta_\rho + \beta(\nu)\cos\theta\eta_\psi + \eta_0 = -\beta(\nu)\sin\theta + \eta_{tot}, \quad (3.9)$$

where the variance of the total noise is

$$\langle\eta_{tot}^2\rangle \equiv \sigma_{tot}^2 = [\sigma\beta'(\nu)\sin\theta]^2 + [\sigma\beta_{-1}(\nu)\cos\theta]^2 + \sigma_0^2, \quad (3.10)$$

with $\beta'(\nu) = \partial\beta(x)/\partial x|_{x=\nu}$ and $\beta_{-1}(\nu) = \beta(\nu)/\nu$. The first term in Eq. (3.10) describes the fluctuations arising from ρ, the amplitude of the gradient estimate, while the second term describes the fluctuations in ψ, the direction of the gradient estimate. Both of them vary with the instantaneous direction of motion $\theta(t)$ and therefore are multiplicative fluctuations. Since the cell responds to noise at its current position, the multiplicative noise is defined with the Itô prescription. From the previous expression it is clear that the ultimate directional dependence in σ_{tot}^2 relies on the sign of $\beta'(\nu) - \beta_{-1}(\nu)$. To capture possible nonlinear input-output characteristics of downstream pathways, we assume that $\beta(\nu)$ has a power-law functional form, i.e. $\beta(\nu) = a\nu^b$. We can distinguish between two qualitatively different cases. In the first, $b > 1$, the total variance is of the "$\sin\theta$" type, $\sigma_{tot}^2 = \sigma_0^2 + (\sigma\beta_{-1})^2 + (\beta'^2 - \beta_{-1}^2)(\sigma\sin\theta)^2$ and is maximal at $\theta = \pi/2$; in the second, $b < 1$, the variance is described by a "$\cos\theta$" type and is maximal at $\theta = 0$. In the special case $b = 1$, the total variance is reduced to $\sigma_{tot}^2 = \sigma_0^2 + a^2\sigma^2$ with no directional dependence.

3.3 Results

We first study the case of $b > 1$ where the restoring force is ultra-sensitive to the input signal. Define the direction-independent noise $\sigma_\perp^2 = \sigma_0^2 + (\sigma\beta_{-1})^2$ and

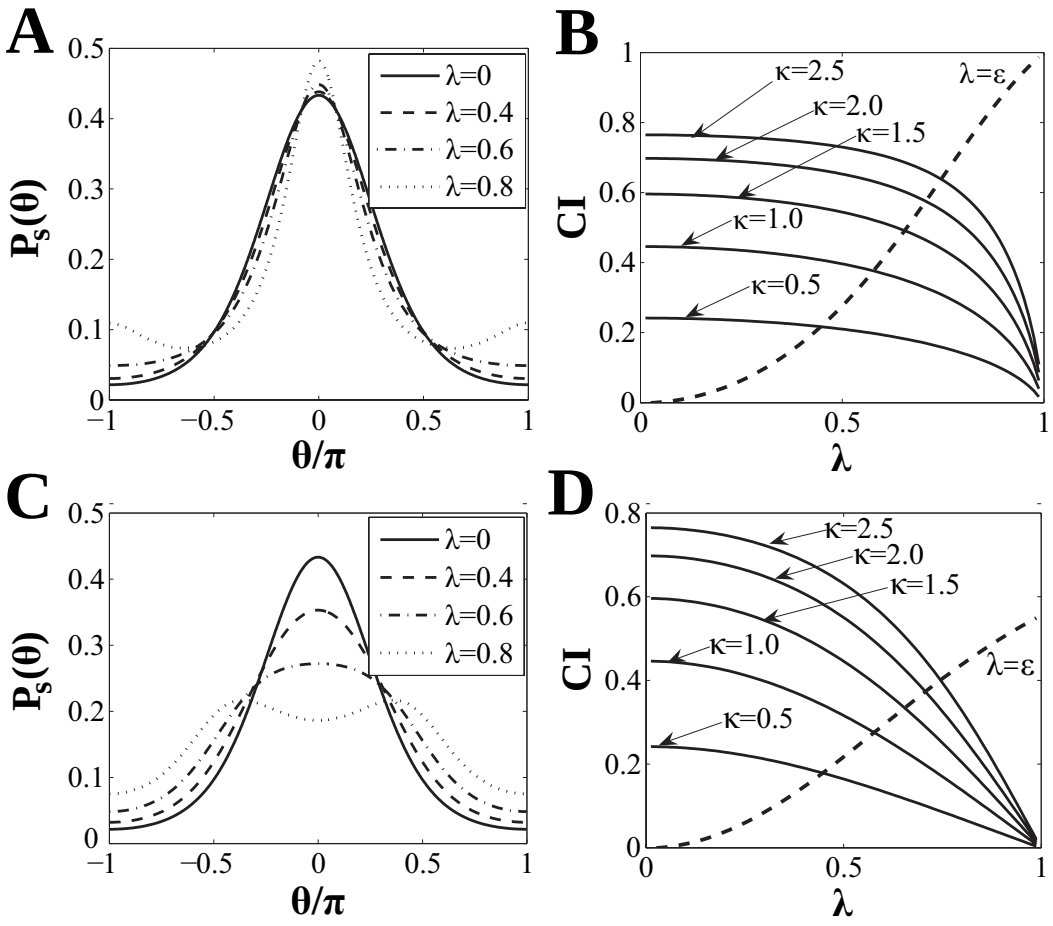


Figure 3.3: The stationary distribution $P_s(\theta|\phi = 0; \kappa = 1.5, \lambda)$ for (A) $b > 1$ and (C) $b < 1$ as a function of the parameter λ representing the ratio of direction-dependent noise to maximal total variance. The chemotaxis index (CI) vs. λ for (B) $b > 1$ and (D) $b < 1$, with the dashed lines indicating where the bifurcation occurs.

the direction-dependent noise $\sigma_\parallel^2 = (\beta'^2 - \beta_{-1}^2)\sigma^2$. Then the previous Langevin equation can be approximated as the Itô SDE

$$\frac{d\theta}{dt} = -\beta(\nu)\sin\theta + \sqrt{(\sigma_\parallel \sin\theta)^2 + \sigma_\perp^2}\,\eta(t), \tag{3.11}$$

where $\eta(t)$ is white noise. One can solve the associated Fokker-Planck equation on the interval $[-\pi, \pi]$ by imposing periodic boundary conditions [18]. The stationary distribution reads

$$P_s(\theta) = \frac{\Omega \exp\left[\kappa \frac{1-\lambda^2}{\lambda} \operatorname{arctanh}(\lambda\cos\theta)\right]}{1 - (\lambda\cos\theta)^2}, \tag{3.12}$$

where $\kappa = 2\beta/\sigma_\perp^2$ is a parameter that compares the direction-biased force with the direction-independent noise and where $\lambda = \sigma_\parallel/\sqrt{\sigma_\parallel^2 + \sigma_\perp^2}$ is the ratio of the direction dependent and maximal total variance. The normalization parameter Ω can be determined numerically. For a vanishing λ, we recover the Circular Normal (CN) distribution:

$$\lim_{\lambda\to 0} P_s(\theta;\kappa,\lambda) = \frac{\exp(\kappa\cos\theta)}{2\pi I_0(\kappa)}. \tag{3.13}$$

For large λ, our stationary distribution will appreciably deviate from the CN distribution with a sharper peak at $\theta = 0$ and heavier tails near $\theta = \pm\pi$ (see Fig. 3.3A). A physical interpretation of this leptokurtic feature can be given by realizing that the first term in the Langevin equation Eq. (3.8) functions as a restoring force. Contrary to the CN case, the amplitude of this force, $\beta(\rho)$, is taken from a distribution. Thus, large values can occur and correspond to large restoring forces which lead to a sharper peak in $P_s(\theta)$. Using the same argument, one can see that the occurrence of small values in this distribution are responsible for the heavy tails in $P_s(\theta)$.

We can further explore the extrema and directionality of $P_s(\theta)$ by recalling that $\operatorname{arctanh}(x) = \frac{1}{2}\ln(\frac{1+x}{1-x})$ and setting $\epsilon \equiv \kappa(1-\lambda^2)/(2\lambda) = \lambda\beta(\nu)/\sigma_\parallel^2$, after which we obtain the alternative form

$$P_s(\theta) = \Omega \frac{(1+\lambda\cos\theta)^{\epsilon-1}}{(1-\lambda\cos\theta)^{\epsilon+1}}. \tag{3.14}$$

The solution of $\partial_\theta \ln P_s = 0$ contains five possible roots on the interval $[-\pi, \pi]$: $\theta = 0$, $\pm\pi$, and $\pm\arccos(-\epsilon/\lambda)$ which exist only if $\lambda > \epsilon$. As seen in Fig. 3.3A,

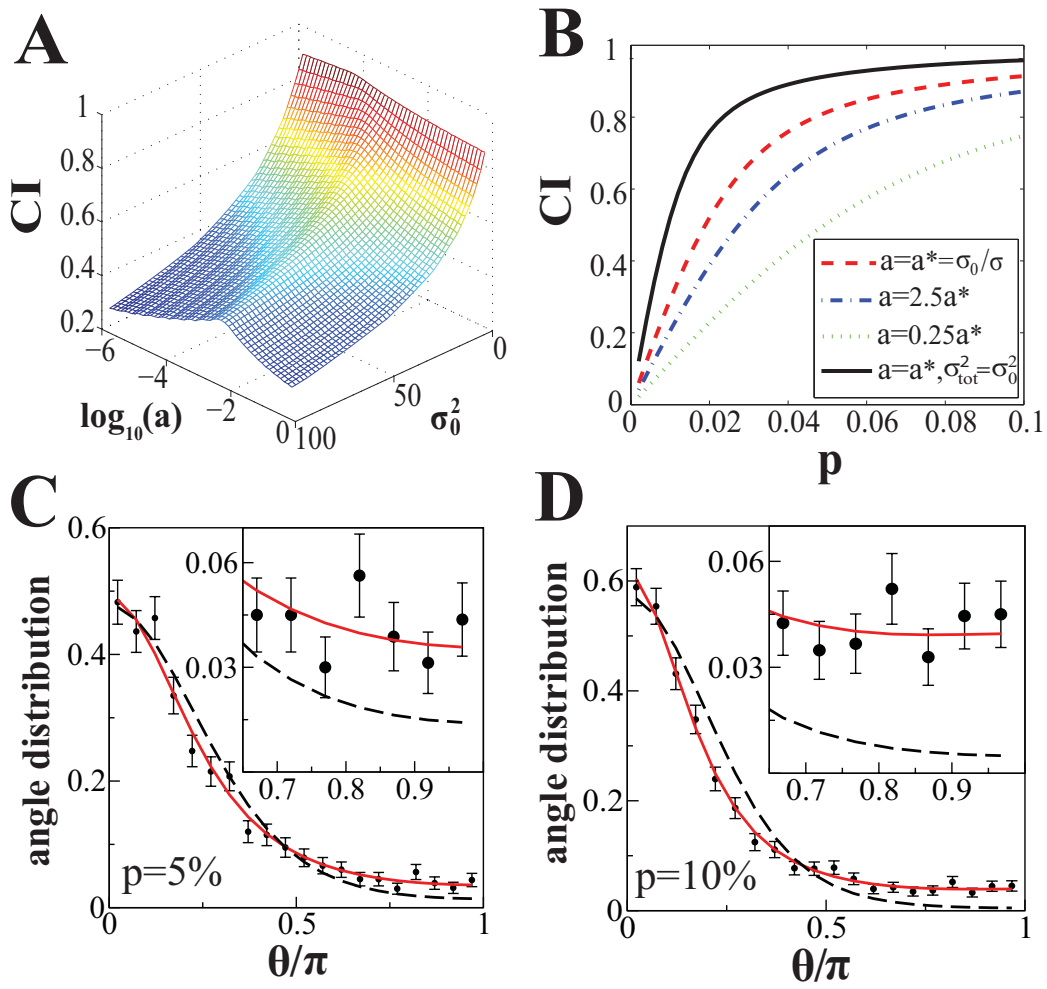


Figure 3.4: Optimal chemotaxis index and fitting of our model to experimental data. (A) CI maximized by choosing appropriate b for different values of a and σ_0^2, given $p = 5\%$ and $C_0 = K_d = 30nM$. (B) CI vs. p for $C_0 = K_d = 30nM$, $\sigma_0^2 = 2$, $b = 1$, and $a = a^*$, $2.5a^*$, and $0.25a^*$. The solid line corresponds to a model neglecting receptor noise, i.e. $\sigma_{tot}^2 = \sigma_0^2$. (C) Experimental direction distribution (symbols) for $p = 5\%$, along with a fit using our model (solid line) and the CN distribution (dashed line). The error bars represent the standard deviation in the data set. The least square fitting parameters are $\lambda = 0.5866$, $\kappa = 1.0222$. (D) Same as (C), but now for $p = 10\%$ and with fitting parameters $\lambda = 0.7566$, $\kappa = 1.8580$. The insets show the tails of the distributions.

$P_s(\theta = \pm\pi)$ correspond to global minima if $\lambda < \epsilon$, but become local maxima once $\lambda > \epsilon$, in which case the new global minima are located at $\theta = \pm \arccos(-\epsilon/\lambda)$. This change of extrema occurs at a critical point $\lambda_c = \epsilon$ (equivalent to $\sigma_{\parallel}^2 = \beta$) where the direction-dependent noise becomes comparable to the magnitude of the restoring force. Direct numerical simulations of the full model described by Eq. (3.8) indicate that our analytical expression for $P_s(\theta)$ works well when SNR$>$ 3 and $\lambda < \epsilon$, justifying the Gaussian noise approximation.

As is common in the experimental literature, we can define an order parameter $\langle \cos\theta \rangle$, the Chemotaxis Index (CI), which is a measure of the directionality of the angular distribution. In Fig. 3.3B, we plot the CI for different values of κ using our model. The dashed line in Fig. 3.3B corresponds to the CI with a value of κ that satisfies the critical condition $\lambda = \epsilon$ or equivalently $\kappa = 2\lambda^2/(1-\lambda^2)$. To the right of this line the distribution shows a local maximum at $\pm\pi$. The slope of the CI is close to 0 over a large range of values for λ. This can be understood by realizing that the negative effect of the heavy tails on the CI is partially compensated by the positive effect of a sharpened peak.

Next we look at the case of $b < 1$. The corresponding stationary distribution is

$$P_s(\theta) = \frac{\Omega \exp\left[\kappa \frac{1-\lambda^2}{\lambda} \arctan(\lambda \cos\theta)\right]}{1 + (\lambda\cos\theta)^2}. \tag{3.15}$$

with $\sigma_{\perp}^2 = \sigma_0^2 + (\sigma\beta')^2$ and $\sigma_{\parallel}^2 = (\beta_{-1}^2 - \beta'^2)\sigma^2$ in the definitions for κ and λ. The analysis proceeds as above and we only highlight the differences. The angle distribution exhibits not only heavy tails but also an obtuse peak for increasing values of λ (Fig. 3.3C). This can be understood since in this case the noise in ψ, i.e. the second term in Eq. (3.10), dominates and reduces the accuracy in directionality. Due to the Gaussian approximation, the analytical probability distribution exhibits double peaks at $\theta = \pm \arccos(-\epsilon/\lambda)$ when $\lambda > \epsilon$ [19]. Also, the CI decays quickly with increasing λ even before the bifurcation (Fig. 3.3D), suggesting that cells should operate in a regime where $b \geq 1$. Finally, for $b = 1$, the directional dependence in σ_{tot}^2 disappears and the stationary distribution reduces to the CN distribution with shape parameter $\tilde{\kappa} = 2a\nu/(\sigma_0^2 + a^2\sigma^2)$. Obviously, for larger values of the parameter a, the system is more sensitive to the gradient, and more of

the receptor noise is transmitted to the directional output.

For any given a and σ_0^2, there exists a unique value of b that maximizes the CI (Fig. 3.4A). We found numerically that the combination of $a^* = \sigma_0/\sigma$ and $b^* = 1$ optimizes the CI over the whole parameter space (a, b) given the level of σ_0. The optimal pair (a^*, b^*) corresponds to the ridge of the CI surface in Fig 3.4A. In summary, the exponent b is critical for the chemotactic responses. The optimal output requires $b = 1$, while $b > 1$ is suboptimal and $b < 1$ leads to poor directionality. This can be understood by realizing that when restoring force $\beta(\nu)$ is a nonlinear function (i.e. $b \neq 1$) of the receptor signal ν, the associated sensor noise is modulated to be direction-dependent, which leads to heavy tails in the angle distribution (Fig. 3.3). In other words, there is a significant probability that cells may move in the wrong direction and the chemotactic performance is not optimal. An important implication of our model is that the CI is always lower than that predicted by models neglecting receptor noise (see Fig. 3.4B). In fact, previous experimental data indicates that when the gradient steepness increases the saturating value of the CI is less than one [5, 9]. This feature is not consistent with previous CN models but may be successfully explained by our $b > 1$ model where the total noise σ_{tot}^2 becomes an increasing function of p.

We can compare our model to the results of recent experiments in which *Dictyostelium* cells were exposed to stable exponential chemoattractant profiles [4]. The data allow us to compute directional distributions for different gradient parameters. To eliminate the slight asymmetric bias introduced by the flow in the microfluidic chambers we collected the data into 20 bins according to their absolute deviation from the gradient direction, $|\theta - \phi|$. The resulting distribution are shown as symbols for $p = 5\%$ and $p = 10\%$ in Fig. 3.4C and 3.4D, respectively. We have also plotted as a solid line a least squares fit to the data using Eq. (3.12) of our model. Our fit captures well the heavy tails and the sharp peaks, features that the CN distribution, plotted as a dashed line, is unable to reproduce. A goodness of fit analysis using the Pearson's chi-square test revealed that the CN distribution is rejected at a significance level of less than 1% while our model exhibits large p-values. For $p = 5\%$, the chi-square test of our model results in $\chi_{our}^2 = 14.14$, with

a degree of freedom DF $= 20 - 3 = 17$ and a p-value equal to 0.657. Here, the DF is reduced by 3 since the model has two fitting parameters and the number of data points is constrained. For comparison, the CN distribution gives $\chi^2_{CN} = 81.54$ with DF $= 18$ and p-value$< 10^{-3}$. For $p = 10\%$, we find $\chi^2_{our} = 10.51$, p-value$= 0.881$, and $\chi^2_{CN} = 694.78$, p-value$< 10^{-3}$. The observed leptokurtic feature suggests that *Dictyostelium* cells are operating close to the optimal regime with the exponent b estimated to be slightly larger than 1.

3.4 Discussion

Eukaryotic cells are capable of detecting small chemical gradients for a wide range of background concentrations. Ultimately, fluctuations place a limit on gradient sensing and recent work has focused on the role of stochastic receptor occupancy as one possible limiting factor. Here, we use a phenomenological approach to add spontaneous motility fluctuations to receptor noise and predict the directional statistics of eukaryotic chemotaxis. Specifically, an Itô diffusion equation with direction-dependent multiplicative noise is developed and analytically studied. We show that our approach can naturally accommodate recent experimental data for the chemotaxis of the social amoeba *Dictyostelium*.

A key assumption in our model is that the chemotaxing cell experiences a relatively stable gradient steepness ($p = const$) regardless of the cell's location or moving history. Thus, our model results can be directly compared to experiments in which the gradient is carefully quantified and controlled. If the gradient steepness is spatially varying, the chemotactic response would be heterogeneous in space, possibly obscuring the structure of the angular distribution.

Although we focus here on the role of receptor noise, it is easy to extend our model to include extra gradient-dependent fluctuations, by adding them to the magnitude of the restoring force, $\beta(\rho)$. Such fluctuations might arise from noise in the downstream signal transduction pathways. Future work will track cells for longer periods of time and test for the presence of long-lived cell individuality and other fluctuations sources [20]. Should the data indicate such memory effects, our

model could be extended to include quenched fluctuations in cell responses.

3.5 Acknowledgements

Chapter 3, in part, is the published material as it appears in Physical Review E, (2010), Hu, Bo; Fuller, Danny; Loomis William F.; Levine, Herbert; Rappel, Wouter-Jan. The dissertation author was the primary investigator and author of this paper.

Bibliography

[1] P.J.V. Haastert and P.N. Devreotes, Nat. Rev. Mol. Cell Biol. **5**, 626 (2004).

[2] C.A. Parent and P.N. Devreotes, Science. **284**, 765 (1999).

[3] L. Song, S.M. Nadkarni, H.U. Bödeker, C. Beta, A. Bae, C. Franck, W.-J. Rappel, W.F. Loomis, and E. Bodenschatz, Eur. J. Cell Biol. **85**, 981 (2006).

[4] D. Fuller, W. Chen, M. Adler, A. Groisman, H. Levine, W.J. Rappel, W.F. Loomis, Proc. Natl. Acad. Sci. U.S.A. **107**, 9656 (2010).

[5] P.J.V. Haastert and M. Postma, Biophys. J. **93**, 1787 (2007).

[6] K. Wang, W.-J. Rappel, R. Kerr, and H. Levine, Phys. Rev. E **75**, 061905 (2007).

[7] W.-J. Rappel and H. Levine, Phys. Rev. Lett. **100**, 228101 (2008).

[8] W.-J. Rappel and H. Levine, Proc. Natl. Acad. Sci. U.S.A. **105**, 19270 (2008).

[9] R.G. Endres and N.S. Wingreen, Proc. Natl. Acad. Sci. U.S.A. **105**, 15749 (2008).

[10] W. Bialek and S. Setayeshgar, Proc. Natl. Acad. Sci. U.S.A. **102**, 10040 (2005).

[11] T. Shibata and K. Fujimoto, Proc. Natl. Acad. Sci. U.S.A. **102**, 331 (2005).

[12] M. Ueda and T. Shibata, Biophys. J. **93**, 11 (2005).

[13] L. Li, S.F. Nørrelykke, and E.C. Cox, PLoS ONE, **3**, e2093 (2008).

[14] H. Takagi, M.J. Sato, T. Yanagida, and M. Ueda, PLoS ONE, **3**, e2648 (2008).

[15] M. Schienbein, K. Franke, and H. Gruler, Phys. Rev. E **49**, 5462 (1994).

[16] D.A. Lauffenburger and J.J. Liderman, *Receptors: Models for Binding, Trafficking, and Signaling* (Oxford University Press, New York, 1993).

[17] H. Gudbjartsson and S. Patz, Magn. Reson. Med. **34**, 910 (1995).

[18] H. Risken, *Fokker-Planck Equation* (Springer-Verlag, Berlin, 1984).

[19] B.W. Andrews and P.A. Iglesias, PLoS Comput. Biol. **3**, e153 (2007).

[20] A. Samadani, J. Mettetal, and A. van Oudenaarden, Proc. Natl. Acad. Sci. U.S.A. **103**, 11549 (2006).

Chapter 4

Input Noise in a Biological Switching System

4.1 Introduction

A broad range of biological processes are regulated by certain switching systems where biochemical molecules randomly flip between on and off states under the regulation of other molecules (kinases, ligands, *etc.*). For example, gene transcription depends on whether DNA promoters are occupied by specific transcription factors [1, 2, 3]; in eukaryotic chemotaxis, accurate sensing of chemical gradients is achieved by using chemoreceptors to detect spatial differences in chemical concentrations [4]. Very often, the number of input molecules is quite small and the stochasticity of input signal, due to molecular diffusion [5] or random births and deaths of molecules [6], is not negligible. This leads to a central question: what is the role of input noise in a biochemical switching system. Previous studies on this topic mostly used the Langevin approach with a linear-noise approximation and/or the fluctuation-dissipation theorem [6, 7, 8, 9, 10, 11, 12, 13, 14, 15, 16], which facilitated a widely accepted view that the input noise will contribute additively to the output variations. These approaches, however, require the assumption that the fluctuations of input signals are very small such that one can linearize the input noise in the chemical Langevin equation. Such a Taylor-expansion treatment

guarantees the *additive noise rule*, i.e., the variance of the output is the sum of the intrinsic variance of the switch and a contribution from the extrinsic input noise.

4.2 Model and Results

Here, we study a simple two-state switch governed by a fluctuating chemical input. Our treatment does not rely on the aforementioned approximations, but instead on exact solutions of the master equation. To explicitly consider the discreteness and randomness of the number of input molecules, we model the input signal $X(t)$ as generated from a simple birth-death process (Fig. 4.1A), where the birth and death rates are denoted by α and β, respectively. Solving the master equation for this process, one can easily find the equilibrium distribution of the input molecules, denoted by C_n, is Poisson with mean $\mu \equiv \alpha/\beta$ and variance $\sigma^2 \equiv \alpha/\beta = \mu$, i.e.,

$$C_n(X(t \to \infty) = n) = \frac{\mu^n}{n!} e^{-\mu}. \tag{4.1}$$

This suggests that $X(t)$ is both nonnegative and mean-reverting. One can also find the stationary covariance, $\lim_{t\to\infty}\langle X(t), X(t+s)\rangle = \sigma^2 e^{-\beta|s|}$. Therefore, $X(t)$ is a stationary Markov process with the relaxation time β^{-1}. It is convenient to choose a time scale by setting $\beta = 1$, so that both the mean and variance of $X(t)$ are determined by α (i.e., $\alpha = \mu = \sigma^2$). Then, we have $\alpha = \mu^2/\sigma^2$, which can be interpreted as the *signal-to-noise ratio*.

We assume that the number of input particles, $X(t)$, directly regulates the transition rates of a downstream switch, the states of which in continuous time constitute the output process, $Y(t)$. For the simplest reaction scheme (Fig. 4.1A), the rate for the molecular switch to turn on is given by $k_{\text{on}}X(t)$ and the rate for it to turn off is k_{off}. Let $P_n(t)$ (and $Q_n(t)$) be the probability to find the switch in the on (and off) state together with exactly n input molecules at time t. Since the input birth-death dynamics is independent of the switch states, we must have $P_n + Q_n = C_n$. Although $Y(t)$ alone is not Markovian, the joint process $(X(t), Y(t))$

is. We can write down the joint master equations for P_n and Q_n as

$$\frac{dP_n}{dt} = k_{\rm on} n Q_n - k_{\rm off} P_n + \alpha P_{n-1} - \alpha P_n + (n+1) P_{n+1} - n P_n, \quad (4.2)$$

$$\frac{dQ_n}{dt} = k_{\rm off} P_n - k_{\rm on} n Q_n + \alpha Q_{n-1} - \alpha Q_n + (n+1) Q_{n+1} - n Q_n. \quad (4.3)$$

In equilibrium, from $Q_n \equiv C_n - P_n$ and Eq. (4.2), we get the following difference equation

$$(k_{\rm on} n + k_{\rm off} + \alpha + n) P_n - \alpha P_{n-1} - (n+1) P_{n+1} = k_{\rm on} n C_n = k_{\rm on} \frac{\alpha^n}{(n-1)!} e^{-\alpha}, \quad (4.4)$$

which reduces to $P_1 = (k_{\rm off} + \alpha) P_0$ at $n = 0$. Thus, if we find the solution for P_0, the expression of P_1 immediately follows and the general solution for P_n is easily determined by Eq. (4.4). We introduce the generating function, $G(z) = \sum_{n=0}^{\infty} z^n P_n$, to transform Eq. (4.4) into

$$(k_{\rm on} + 1) z G' + (k_{\rm off} + \alpha) G - \alpha z G - G' = k_{\rm on} \alpha z e^{\alpha(z-1)}, \quad (4.5)$$

which contains a regular (power-law) singular point at $z_s \equiv (k_{\rm on} + 1)^{-1}$, so that generically,

$$G(z) \sim (z - z_s)^{-\lambda}, \qquad \lambda \equiv z_s (k_{\rm off} + \alpha - \alpha z_s). \quad (4.6)$$

Choosing the boundary condition to eliminate the possible singularity at z_s, we find an integral solution:

$$G(z) = \int_{z_s}^{z} \frac{k_{\rm on} \alpha e^{-\alpha} z_s x}{x - z_s} \left| \frac{x - z_s}{z - z_s} \right|^h \exp\left(\frac{k_{\rm on} \alpha x + \alpha z}{k_{\rm on} + 1} \right) dx \quad (4.7)$$

where $h \equiv z_s^2 (k_{\rm on} k_{\rm off} + k_{\rm on} \alpha + k_{\rm off})$. In particular, this directly gives $P_0 = G(z = 0)$. Moreover, the equilibrium probability to find the switch in the on state is given by $P_{\rm on} = \sum_{n=0}^{\infty} P_n = G(z = 1)$, which we will examine for different limits later on.

If the input is fixed at a constant level (i.e. $X(t) = \alpha$), the output $Y(t)$ is clearly a two-state Markov (or random telegraph) process with the forward rate, $K_+ \equiv k_{\rm on} \alpha$, and the backward rate, $K_- \equiv k_{\rm off}$. Since $k_{\rm off}$ is independent of $X(t)$, the input noise will only affect the chance for the switch to turn on. One can calculate the mean waiting time, τ_n, for the switch to turn on given that it starts from being off with n particles initially. We first write the backward Kolmogorov

equation for $\rho_n(t)$, which denotes the probability density for the switch (starting with n particles) to exit the off state at time t:

$$\rho_n(t) = \left[1 - (\alpha + n + k_{\text{on}} n)\, dt\right] \rho_n(t-dt) + \alpha\rho_{n+1}(t-dt)dt + n\rho_{n-1}(t-dt)dt + k_{\text{on}} n\delta(t), \tag{4.8}$$

where the first term represents the probability of nothing happening so that the exit has to be at $t-dt$, the second the probability that there is currently a birth so that the exit has to be at $t-dt$ from the $n+1$ particle state, the third the probability that there is a death, and the last term represents the boundary condition using the Dirac delta function. This equation can be expanded and reorganized to the following differential equation,

$$\frac{d\rho_n}{dt} = -\left(\alpha + n + k_{\text{on}} n\right) \rho_n + \alpha\rho_{n+1} + n\rho_{n-1} + k_{\text{on}} n\delta(t). \tag{4.9}$$

To calculate the mean first passage time, we multiply both sides of Eq. (4.9) by t and integrate over all t, yielding

$$\left(\alpha + n + k_{\text{on}} n\right) \tau_n = \alpha\tau_{n+1} + n\tau_{n-1} + 1. \tag{4.10}$$

By defining $f_n \equiv \tau_n \alpha^n / n!$, Eq. (4.10) can be simplified as

$$\left(k_{\text{on}} n + n + \alpha\right) f_n - (n+1) f_{n+1} - \alpha f_{n-1} = \alpha^n / n! \tag{4.11}$$

which looks quite similar to Eq. (4.4) and can be transformed into a differential equation by introducing $F(z) = \sum_{n=0}^{\infty} z^n f_n$. The solution is immediate:

$$F(z) = \int_{z_s}^{z} \frac{z_s}{x - z_s} \left|\frac{x - z_s}{z - z_s}\right|^{z_s^2 k_{\text{on}} \alpha} \exp\left(\frac{k_{\text{on}} \alpha x + \alpha z}{k_{\text{on}} + 1}\right) dx. \tag{4.12}$$

The mean waiting time in equilibrium for the switch to turn on is

$$\begin{aligned} \overline{\tau} &= \sum_n \tau_n C_n = \sum_n f_n e^{-\alpha} = F(1) e^{-\alpha} \\ &= \int_{z_s}^{1} \frac{e^{-\alpha} z_s}{x - z_s} \left(\frac{x - z_s}{1 - z_s}\right)^{z_s^2 k_{\text{on}} \alpha} \exp\left(\frac{k_{\text{on}} \alpha x + \alpha}{k_{\text{on}} + 1}\right) dx. \end{aligned} \tag{4.13}$$

In the slow switch limit ($k_{\text{on}}\alpha \ll \beta = 1$), we can evaluate the integral of Eq. (4.13) by expanding its exponential term around $k_{\text{on}}\alpha$. To leading order, this gives

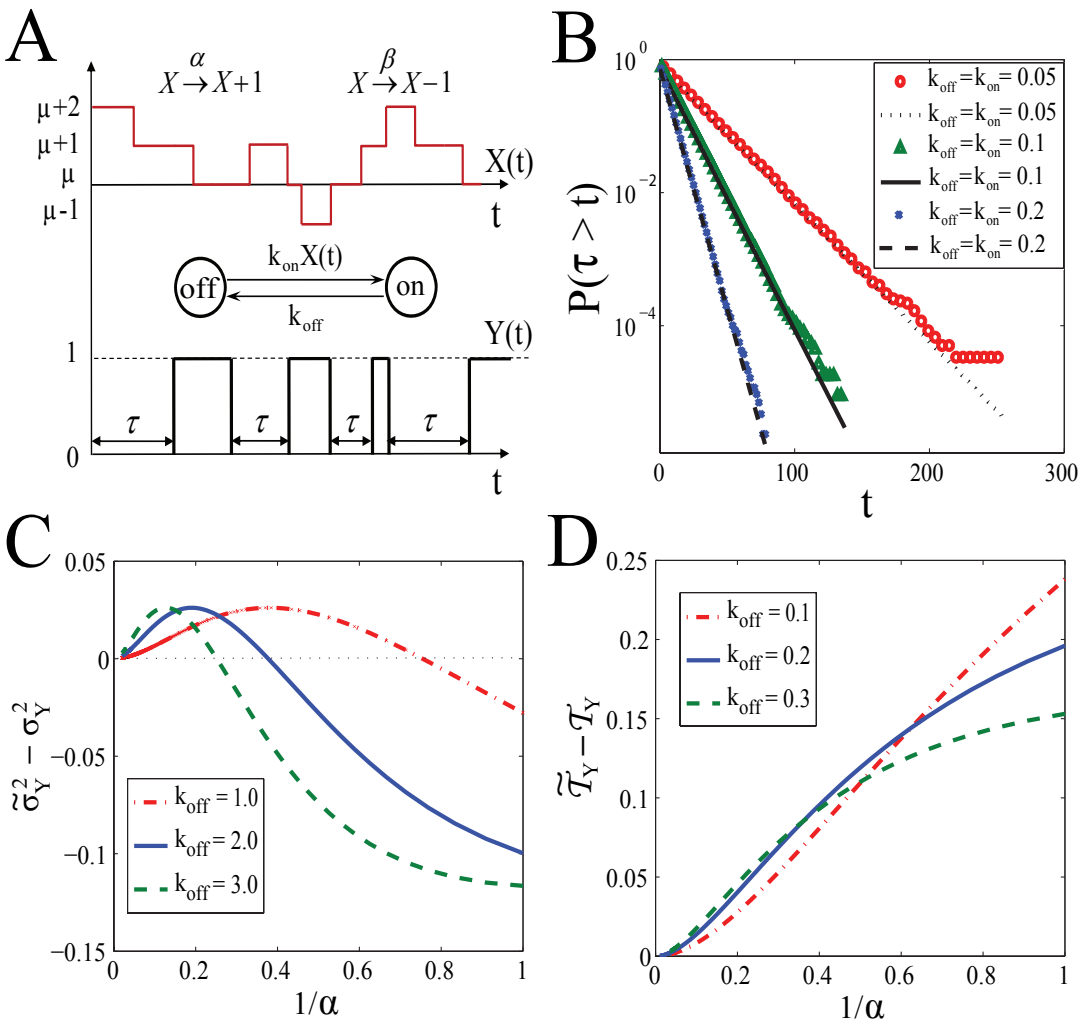


Figure 4.1: Analytical and numerical results in the slow switch limit. (A) Schematic representation of our model. (B) $P(\tau > t)$ versus t, with fixed $\alpha = 1$ and $\beta = 1$ but different $k_{\rm on}$ and $k_{\rm off}$. Symbols represent simulation results, while lines denote $P(\tau > t) = \exp(-\widetilde{k}_{\rm on}\alpha t)$. (C) $\widetilde{\sigma}_Y^2 - \sigma_Y^2$ versus $1/\alpha$ from theory, where we choose $\beta = 1$, $k_{\rm on} = 1$, and different values of $k_{\rm off}$. (D) $\widetilde{\mathcal{T}}_Y - \mathcal{T}_Y$ versus $1/\alpha$ from theory, for $\beta = 1$, $k_{\rm on} = 0.1$, and different $k_{\rm off}$.

$\overline{\tau} \approx (z_s k_{\text{on}}\alpha)^{-1}$, which is obviously larger than the average time, $K_+^{-1} = (k_{\text{on}}\alpha)^{-1}$, for the on transition in the constant input model. Thus, for our noisy input model, we can define an effective on rate, $\widetilde{k}_{\text{on}} \equiv z_s k_{\text{on}}$. Correspondingly, we can define an effective forward rate $\widetilde{K}_+ \equiv \widetilde{k}_{\text{on}}\alpha$ which, in terms of K_+, can be written as:

$$\widetilde{K}_+ \equiv z_s K_+ = \frac{\alpha K_+}{\alpha + K_+} = \left(\frac{1}{\alpha} + \frac{1}{K_+}\right)^{-1} < K_+. \tag{4.14}$$

To analyze the effect of input noise, we vary α and simultaneously fix the forward rate $K_+ = k_{\text{on}}\alpha$ such that the mean on-state occupancy for the constant input model, $K_+/(K_- + K_+)$, remains constant. In contrast, the mean on-state occupancy for our noisy input model is $\widetilde{K}_+/(K_- + \widetilde{K}_+)$ which is less than $K_+/(K_- + K_+)$ by Eq. (4.14). This means that the input noise will effectively suppress the on state by prolonging the average time for the switch to turn on. The larger the noise, the more the suppression. Our Monte-Carlo simulations reveal that the switch's off-state residence times (τ) are still, to good approximation, distributed exponentially, $P(\tau > t) \approx \exp(-\widetilde{k}_{\text{on}}\alpha t)$, as shown in Fig. 4.1B. Thus, $Y(t)$ in this case can be well approximated as a two-state Markov process with transition rates $\widetilde{k}_{\text{on}}\alpha$ and k_{off}. Likewise, we can evaluate $P_{\text{on}} = G(1)$ by Taylor expansion in this slow switch limit, yielding

$$P_{\text{on}} \approx \frac{k_{\text{on}}\alpha}{k_{\text{on}}k_{\text{off}} + k_{\text{on}}\alpha + k_{\text{off}}} = \frac{\widetilde{k}_{\text{on}}\alpha}{\widetilde{k}_{\text{on}}\alpha + k_{\text{off}}}, \tag{4.15}$$

consistent with the result $\overline{\tau} \approx 1/(\widetilde{k}_{\text{on}}\alpha)$. So the variance of $Y(t)$ is $\widetilde{\sigma}_Y^2 = P_{\text{on}}(1 - P_{\text{on}}) \approx \widetilde{k}_{\text{on}}\alpha k_{\text{off}}/(\widetilde{k}_{\text{on}}\alpha + k_{\text{off}})^2$. In contrast, the output variance for the constant-input model is $\sigma_Y^2 = k_{\text{on}}\alpha k_{\text{off}}/(k_{\text{on}}\alpha + k_{\text{off}})^2$. Their difference $\widetilde{\sigma}_Y^2 - \sigma_Y^2$ is plotted as a function of α^{-1} in Fig. 4.1C. For small noise ($\alpha = \mu^2/\sigma^2 \gg 1$), we find approximately

$$\widetilde{\sigma}_Y^2 - \sigma_Y^2 \approx \frac{k_{\text{off}}[k_{\text{on}}\alpha - 2k_{\text{off}}(2 + k_{\text{on}})]}{k_{\text{on}}\alpha^2} + \mathcal{O}\left(\frac{1}{\alpha^3}\right). \tag{4.16}$$

Eq. (4.16) tells that the input noise (controlled by α^{-1}) does not always contribute additively to the output variance $\widetilde{\sigma}_Y^2$. The contribution can be even negative when $\alpha < 2k_{\text{off}}(1 + 2k_{\text{on}}^{-1})$. This seemingly surprising result has a simple explanation: a two-state switch at any moment is just a Bernoulli random variable and hence its

variance is strictly upper bounded by one quarter. From Eq. (4.15) and Fig. 4.1B, one can see that the net effect of input noise is to reduce the on rate slightly from $k_{\rm on}$ to $\widetilde{k}_{\rm on}$. This turns out to be a general feature for any two-state (single) switch system, no matter how the input process is assigned or whether the switch exhibit ultra-sensitive response through cooperativity. We will elaborate on this point elsewhere. Returning to our noisy input model, the output autocorrelation time is $\widetilde{\mathcal{T}}_Y \approx (\widetilde{k}_{\rm on}\alpha + k_{\rm off})^{-1}$, which is obviously larger than $\mathcal{T}_Y \equiv (k_{\rm on}\alpha + k_{\rm off})^{-1}$, the output autocorrelation time for the constant-input model. In the limit $\alpha \gg k_{\rm off}/k_{\rm on}$, we find that $\widetilde{\mathcal{T}}_Y - \mathcal{T}_Y \approx \alpha^{-1} + \mathcal{O}(\alpha^{-2})$. Thus, $\widetilde{\mathcal{T}}_Y$ increases with the relative level of input noise ($\alpha^{-1} = \sigma^2/\mu^2$) when the mean level of X is much larger than the dissociation constant $K_d \equiv k_{\rm off}/k_{\rm on}$; see Fig. 4.1D. Consider an integration of the output signal $Y(t)$ over a time window T (assuming $T \gg \mathcal{T}_Y$). The output variance after temporal averaging becomes:

$$\mathrm{Var}\left(\frac{1}{T}\int_0^T Y(t)dt\right) \simeq \frac{2\widetilde{\mathcal{T}}_Y}{T}\widetilde{\sigma}_Y^2, \tag{4.17}$$

which may still decrease with the relative level of input noise α^{-1}, just as $\widetilde{\sigma}_Y^2$ does (Fig. 4.1C). All the above results show that the *additive noise rule* is an incomplete characterization of the input-output noise relationship for a single switch system. Finally, we calculate the mean number of particles given that the switch is on,

$$N_{\rm on} = \frac{\sum_n nP_n}{\sum_n P_n} = \frac{G'(1)}{G(1)} = \alpha\left(\frac{1}{P_{\rm on}} - \frac{k_{\rm off}}{k_{\rm on}\alpha}\right). \tag{4.18}$$

Using our result for $P_{\rm on}$ in the slow switch limit, we get

$$N_{\rm on} \approx \alpha\left(1 + \frac{k_{\rm off}}{\alpha}\right) = \alpha + k_{\rm off} > \alpha. \tag{4.19}$$

Thus, input noise can increase $N_{\rm on}$ significantly if $k_{\rm off}$ is relatively large. The average number of particles given that the switch is off, denoted by $N_{\rm off}$, is found as well:

$$N_{\rm off} = \frac{\sum_n nQ_n}{\sum_n Q_n} = \frac{\mu - G'(1)}{1 - G(1)} = \frac{k_{\rm off}}{k_{\rm on}}\frac{P_{\rm on}}{1 - P_{\rm on}}, \tag{4.20}$$

which, in the slow switch limit, gives

$$N_{\rm off} \approx K_d\frac{\widetilde{k}_{\rm on}\alpha}{k_{\rm off}} = z_s\alpha = \frac{\alpha}{1 + k_{\rm on}} < \alpha. \tag{4.21}$$

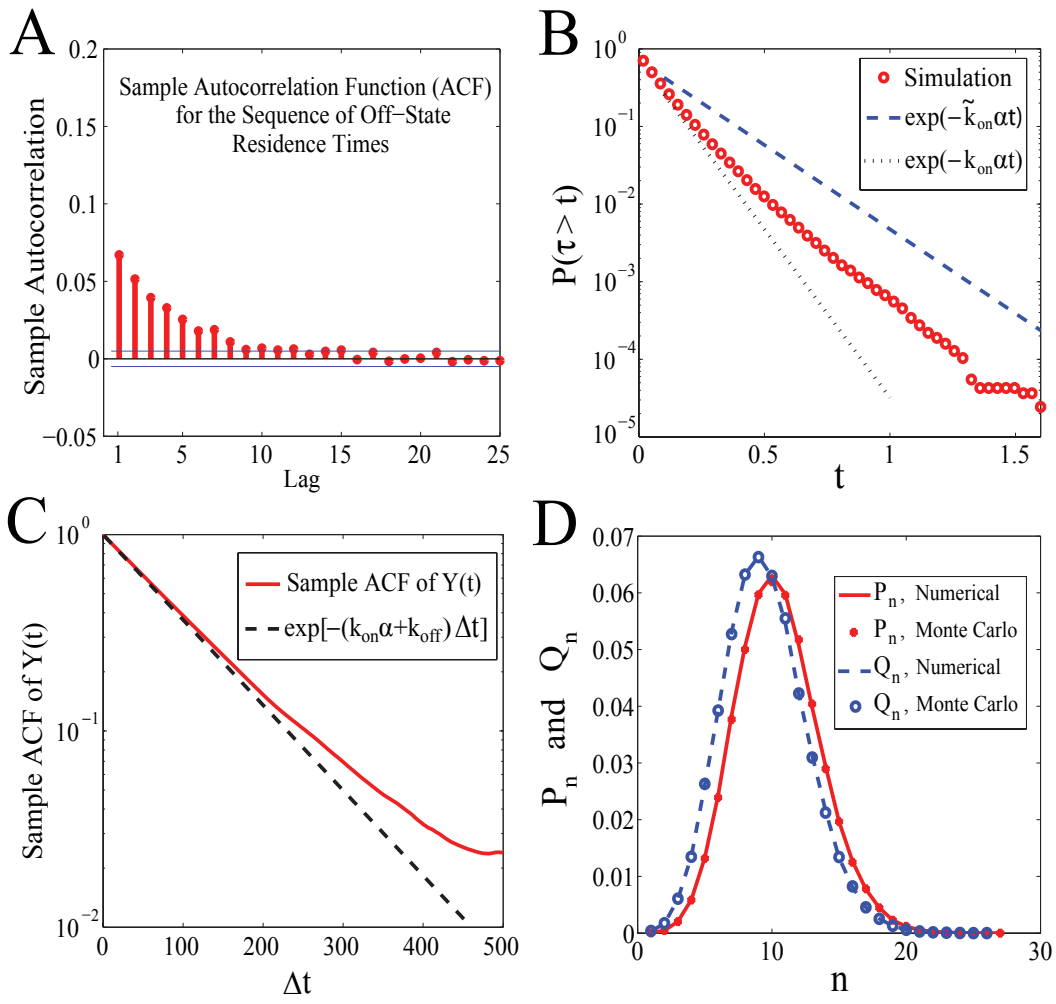


Figure 4.2: Numerical results of our model in the fast switching limit. We choose $\alpha = 10$, $\beta = 1$, $k_{\text{on}} = 1$, and $k_{\text{off}} = 10$. (A) Sample ACF of the sequence of the off-state residence times. (B) Distribution of the off-state residence times. (C) Sample ACF of $Y(t)$. (D) P_n and Q_n versus n.

Thus, we have $N_{\rm off} < N_{\rm on}$ in general.

In the fast switch limit ($k_{\rm on}\alpha \gg \beta = 1$), the approximate expression for Eq. (4.13) is found to be

$$\overline{\tau} \approx \frac{e^{-\widetilde{k}_{\rm on}\alpha}}{\widetilde{k}_{\rm on}\alpha} + \frac{e^{-\widetilde{k}_{\rm on}\alpha}}{k_{\rm on}+1}\left[1 + \sum_{j=1}^{\infty} \frac{(\widetilde{k}_{\rm on}\alpha)^j}{j \cdot j!}\right]. \tag{4.22}$$

For fixed α and $k_{\rm on} \to \infty$, we have $\widetilde{k}_{\rm on} \to 1$ and hence $\overline{\tau} \to e^{-\alpha}/\alpha$ which is just the time to leave the $n = 0$ state times the probability of being in the $n = 0$ state. Looking at the maximal noise limit ($\alpha \ll 1$), we can restrict our attention to $n = 0$ and $n = 1$. This results in a simple Markov chain model where one can easily calculate,

$$P_0 \approx \frac{k_{\rm on}\alpha}{k_{\rm off}^2 + k_{\rm off} + k_{\rm on}\alpha + k_{\rm off}k_{\rm on}}, \tag{4.23}$$

such that the overall probability to find the switch on is

$$P_{\rm on} \approx P_0 + P_1 \approx \frac{(k_{\rm off} + \alpha + 1)k_{\rm on}\alpha}{k_{\rm off}^2 + k_{\rm off} + k_{\rm on}\alpha + k_{\rm off}k_{\rm on}}. \tag{4.24}$$

Unlike the case of a slow switch, the successive off-state residence times are slightly correlated with each other (Fig. 4.2A), as a natural result of the temporal correlation in the input process. The distribution of these off-state residence times, $P(\tau)$, is not exponential (Fig. 4.2B), especially at the head, although its tail decays exponentially at the rate $\widetilde{k}_{\rm on}\alpha$. In Fig. 4.2C, we draw the sample *autocorrelation function* (ACF) for the simulated output path. Clearly, the ACF of $Y(t)$ exhibits a much longer tail than what one expects from the constant input model, demonstrating a long-term memory in $Y(t)$. All the above results (Fig. 4.2A-C) show that the output process $Y(t)$ is strongly non-Markovian in the fast switch limit. As a last illustration of the interdependence of input and output, we plot in Fig. 4.2D the equilibrium conditional distributions, P_n and Q_n, which are obtained by running Monte-Carlo simulations or by numerically solving Eqs. (4.2) and (4.3). Clearly, one can see from Fig. 4.2D that $N_{\rm off} < N_{\rm on}$.

4.3 Discussion

Our results may have broad biological implications. The effects of input noise on the output statistics may be quite different, depending on the input relaxation time scale β^{-1} compared to the typical switching time scale $\mathcal{T}_Y$. The rate β can represent either the degradation of input particles or molecular diffusion which removes input particles from a restricted space for chemical reaction. If molecular diffusion is the biophysical basis for β, then faster diffusion will make the input noise less appreciable, consistent with the Burg-Percell formula for concentration sensing limits [5, 11, 12, 13, 14, 15]. Many biological processes may be classified into this scenario where input fluctuations are of little impact. For example, switching of DNA promoters usually occurs at a time scale much longer than the characteristic diffusion time of transcription factors, providing a temporal averaging opportunity to suppress the input noise. Eukaryotic gradient sensing is another example where the chemoattractant cAMP diffuses so fast that one can ignore the input diffusive noise when considering cellular gradient sensing capacities [13, 16]. Nonetheless, there exist biological situations where the input relaxes much slower than the biochemical switch flips its states. Take for example the bacterial flagellar motors which rotate either clockwise or counterclockwise for chemotactic movements. The probability of clockwise motor spinning depends sharply on the concentration of CheY-P in E. coli [17, 18, 19]. The correlation time of the input CheY-P level is dominated by slow methylation kinetics and measures $10 \sim 30$ seconds [20]. This is much longer than the typical switching time of the flagellar motors which is approximately 1 second [17, 18, 19, 20, 21]. Therefore, input noise in this system is expected to have interesting effects on the motor switching statistics, as experimentally revealed in [17, 18, 19] and theoretically explored in [21].

In summary, we have presented a solvable stochastic model to analyze how input fluctuations affect a simple biochemical switch. Contrary to the common belief, our analysis shows that the presence of input noise does not necessary increase the output variance for a single switch. We also demonstrate that a long-last memory in the input process can bring up non-exponential statistics in

the output switching process. Future research may extend our current model by incorporating other effects like feedback loops and cooperativity.

4.4 Acknowledgements

Chapter 4, in full, is the material which has been submitted for publication and which may appear in Physical Review, (2011), Hu, Bo; Kessler, David A.; Rappel, Wouter-Jan; Levine, Herbert. The dissertation author was the primary investigator and author of this paper.

Bibliography

[1] M.B. Elowitz, A.J. Levine, E.D. Siggia, and P.D. Swain, Science **207**, 1183 (2002).

[2] P.S. Swain, M.B. Elowitz, and E.D. Siggia, Proc. Natl. Acad. Sci. U.S.A. **99**, 12795 (2002).

[3] W.J. Blake, M. Kærn, C.R. Cantor, and J.J. Collins, Nature **422**, 633 (2003).

[4] C.A. Parent and P.N. Devreotes, Science. **284**, 765 (1999).

[5] H.C. Berg and E.M. Purcell, Biophys. J. **20**, 193 (1977).

[6] J. Paulsson, Nature **427**, 415 (2004).

[7] M.L. Simpson, C.D. Cox, and G.S. Saylor, J. Theor. Biol. **229**, 383 (2004).

[8] T. Shibata and K. Fujimoto, Proc. Natl. Acad. Sci. U.S.A. **102**, 331 (2005).

[9] S. Tănase-Nicola, P.B. Warren, and P.R. ten Wolde, Phys. Rev. Lett. **97**, 068102 (2006).

[10] Gašper Tkačik, T. Gregor, and W. Bialek, PLoS ONE **3**, e2774 (2008).

[11] W. Bialek and S. Setayeshgar, Proc. Natl. Acad. Sci. U.S.A. **102**, 10040 (2005).

[12] W. Bialek and S. Setayeshgar, Phys. Rev. Lett. **100**, 258101 (2008).

[13] K. Wang, W.-J. Rappel, R. Kerr, and H. Levine, Phys. Rev. E **75**, 061905 (2007).

[14] R.G. Endres and N.S. Wingreen, Proc. Natl. Acad. Sci. U.S.A. **105**, 15749 (2008).

[15] R.G. Endres and N.S. Wingreen, Phys. Rev. Lett. **103**, 158101 (2009).

[16] B. Hu, W. Chen, W.J. Rappel, and H. Levine, Phys. Rev. Lett. **105**, 048104 (2010).

[17] P. Cluzel, M. Surette, and S. Leibler, Science **287**, 1652 (2000).

[18] E.A. Korobkova, T. Emonet, J.M.G. Vilar, T.S. Shimizu, and P. Cluzel, Nature **428**, 574 (2004).

[19] E.A. Korobkova, T. Emonet, H. Park, and P. Cluzel, Phys. Rev. Lett. **96**, 058105 (2006).

[20] T.S. Shimizu, Y. Tu, and H.C. Berg, Mol. Syst. Biol. **6**, 382 (2010).

[21] Y. Tu and G. Grinstein, Phys. Rev. Lett. **94**, 208101 (2005).

Chapter 5

Mechanisms for Signaling Specificity

5.1 Introduction

Cells are able to reliably execute various functions in response to different environmental conditions. Each function is mediated by a signaling transduction pathway, which converts the external stimulus into specific intracellular signals. These signaling cascades involve intracellular biochemical reactions, carried out by a multitude of second messengers [1, 2]. Often, these cascades cross-activate or share signaling components, raising the possibility of erroneous activation of certain pathways [3]. Examples include pathways involving the second messenger cyclic adenosine monophosphate (cAMP) and mitogen activated protein kinase (MAPK) cascades that regulate multiple functions in eukaryotic cells [4, 5, 6].

To ensure signaling specificity, a variety of strategies can be employed [3]. Physically separating the signaling components, for example through sequestration or compartmentalization, is conceptually the simplest way to avoid undesirable cross-talk [7, 8, 9]. Alternatively, signaling specificity can be promoted by cross-pathway inhibition which redirects the information flow toward appropriate downstream targets [10, 11]. Since cross-talk often occurs at multiple levels of the signaling cascades, it remains a challenge to understand the intricate wiring

required to impart signaling specificity. In particular, it is difficult to determine the minimum number of inhibitory links that are needed to suppress undesired crosstalk, how to organize these links, and how to enumerate the number of possible network configurations that guarantee signaling specificity.

In this study, we address these questions using simple theoretical and numerical tool. In particular, we show that we can capture the essential dynamics of two cross-activating signaling cascades by reducing them to a simplified module that contains only four nodes. Using a genetic algorithm [12, 13], we probe all possible configurations of this module that contain inhibitory links. We find that the unique topology that imparts signaling specificity employs the asymmetric hierarchical inhibition mechanism, in which two inhibitory links operate at different levels of the signaling cascade. We apply this finding to general and complex signaling networks and, after discussing a reduction procedure, enumerate the possible topologies that allow for signaling specificity.

Our approach and results are then applied to the budding yeast *Saccharomyces cerevisiae*, a model system for cross-talk [3]. We focus on its mating and filamentation pathways which are characterized by a number of shared components. After enumerating the number of possible topologies and explicitly determining their network architectures, we show that only two of these topologies are plausible in the light of existing experimental data.

5.2 Results

5.2.1 A four-node module underlies signaling pathways with cross-activation

As a first step, we present a coarse-graining method for signaling networks with crosstalk. An example of two cross-activating pathways is presented in Fig. 5.1A, where the input information is transmitted by a set of signaling components (indicated by nodes) that are connected through a series of biochemical reactions (links). In what follows, a link can represent either the activation (arrow) or the

inhibition (bar) of one component by another. The graph is drawn in a causal way such that time flows from top (or input) to bottom (or output) and shared components can easily be identified.

To reduce the complexity of this signaling network, we first identify the shared component(s) that are responsible for cross-activation. Next, we replace the shared node(s) by a set of cross- and direct activation links. Each of these links connects the node upstream of the shared node(s) to the node downstream of the shared node(s) (Fig. 5.1B). This results in two signaling cascades with possibly multilevel crosstalk, as represented by the activation links across the two cascades. Several subsystems, each of which contains only one pair of cross-pathway links, can be identified (Fig. 5.1B). Concentrating on one of the subsystems, we see that the signaling components of each pathway can be divided into two groups (Fig. 5.1C). One group is composed of pathway-specific components that are activated before any crosstalk in the subsystem, while the second group contains nonspecific components affected by the cross-activation (Fig. 5.1C). A component is pathway-specific if it is only present or significantly activated in one particular pathway; otherwise, it is nonspecific.

The activity of these components can be analyzed using the Boolean logic where a node is either on (1) or off (0). Clearly, the elements in each group are always in the same logical state under all different input conditions, and thus can be combined into a single node. This enables us to consider a reduced "four-node system", in which each input component can activate both of the output components (Fig. 5.1D). The architecture of this coarse-grained four-node topology underlies the original full network. Understanding the functional properties of this basic circuit will provide insight into the signaling specificity of more complex biomolecular circuits.

5.2.2 Asymmetric hierarchical inhibition ensures signaling specificity

The four-node system is made up of two signaling cascades which we will denote X and Y (Fig. 5.2A), with their input and output components labeled by

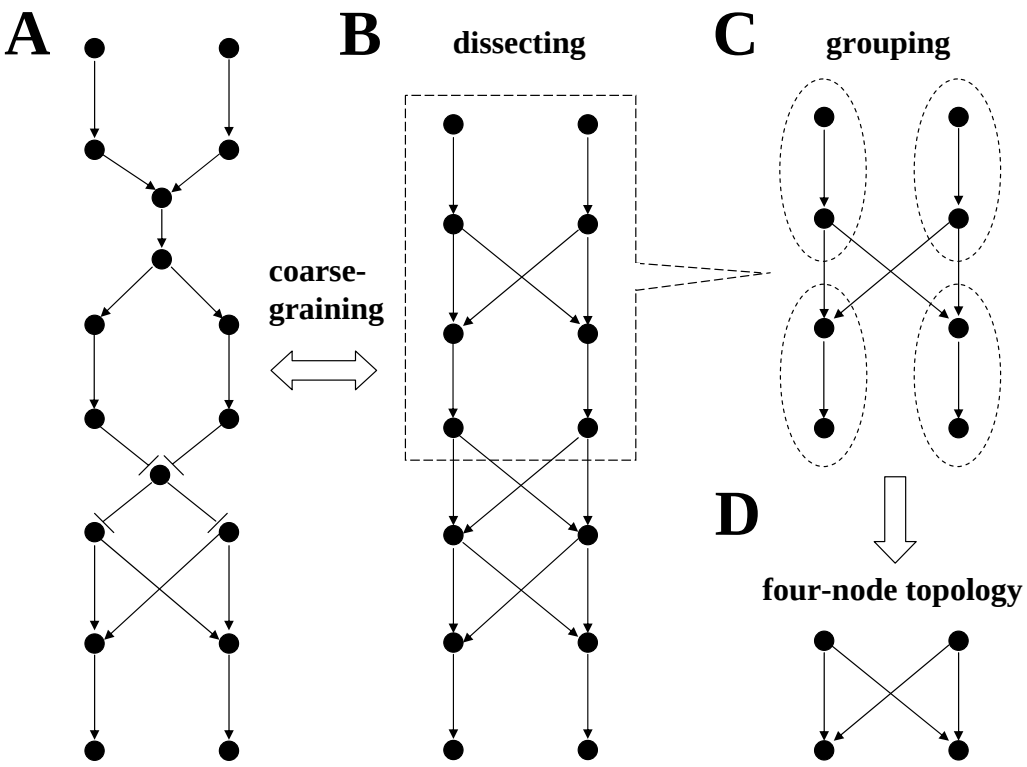
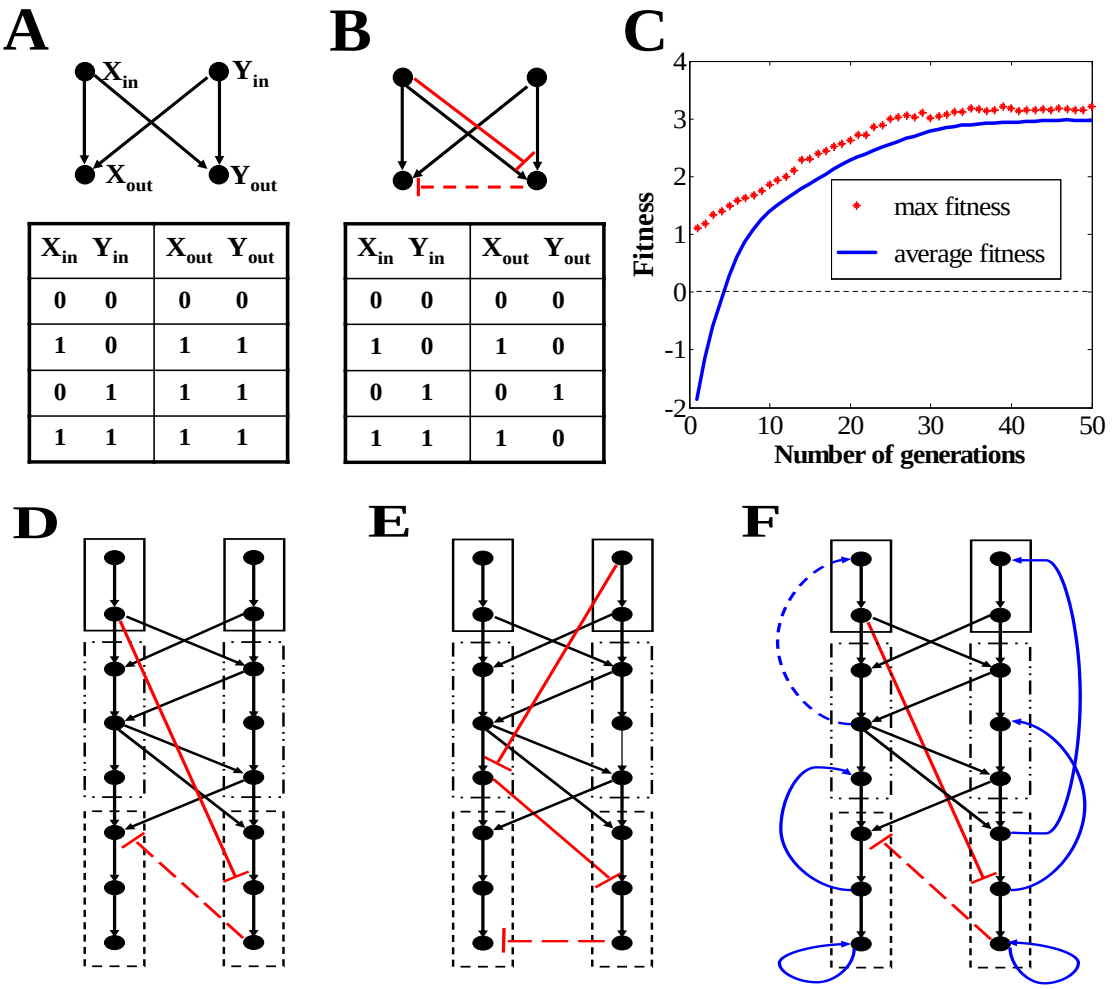


Figure 5.1: A simple four-node topology underlies cross-activating signaling networks. (A) A graphical representation of two typical signaling transduction pathways with shared components at multiple levels. The nodes represent single or groups of biochemical components while the links represent either activation (arrows) or inhibition (bars). (B) After coarse-graining this network, one can dissect the network into several subsystems, each of which contains only one pair of cross-activating links. (C) The nodes in each subsystem can be grouped such that the components have the same logical states (on or off). (D) The final result is a four-node topology, containing two input nodes and two output nodes, along with two cross-activating links.

the subscript "in" and "out", respectively. Without any inhibitory links, this basic system does not exhibit signaling specificity, as reflected in the truth table that reports the output states as a function of the input states (Fig. 5.2A). After all, signaling specificity is achieved if Y_{out} is negligible compared to X_{out} when only X_{in} is stimulated and vice versa. Additional requirement is the mutual exclusiveness in the output when both input signals are stimulated. As a specific example, we will consider here the case where the pathway X is *dominant*, which means in the Boolean logic that $X_{out} = 1$ and $Y_{out} = 0$ given that $X_{in} = 1$ and $Y_{in} = 1$. The corresponding desired truth table is presented in Fig. 5.2B.

Mathematically, the four-node system can be described by four ordinary differential equations; see Materials and Methods for details. In this four-node topology, we can place at most eight inhibitory links (for instance, X_{out} suppressing Y_{out}, X_{in} suppressing Y_{out}, etc.), and hence enumerate in total $2^8 = 256$ possible topologies. To investigate which configurations give rise to the desired function, we devise a genetic algorithm to automatically seek the solution(s). The algorithm starts from a population of random realizations of the eight inhibitory links, with the strength of each link being controlled by a parameter that is chosen at random within a certain range. For each network topology, we evaluate its fitness score based on its input-output characteristics. The fitness score is a quantitative measure of the network's cost-effective capacity to perform the desired signaling function (Materials and Methods). The algorithm then keeps the top 50% best-fit networks as seeds for reproduction in the next generation, where the eight inhibitory links in each seed network are subject to random mutations. This process is repeated until a stable fitness value is achieved.

The maximum fitness score, along with the average fitness, is shown in Fig. 5.2C as a function of the generation number. After roughly 30 generations, the algorithm converges and produces a unique stable topology that contains two inhibitory links (Fig. 5.2B). One of the inhibitory links denotes the suppression of Y_{out} by X_{in} while the other represents the inhibition of X_{out} by Y_{out}. Their combination can be classified as the asymmetric hierarchical inhibition [11]. It is asymmetric since the two inhibitory links break the symmetry of the four-node



X_{in}	Y_{in}	X_{out}	Y_{out}
0	0	0	0
1	0	1	1
0	1	1	1
1	1	1	1

X_{in}	Y_{in}	X_{out}	Y_{out}
0	0	0	0
1	0	1	0
0	1	0	1
1	1	1	0

Figure 5.2: (A) The truth table associated with the basic four-node topology with crosstalk. (B) The inclusion of two inhibitory links, one dominant (solid line) and the other non-dominant (dashed line), leads to an asymmetric hierarchical inhibition mechanism and a truth table that exhibits signaling specificity and mutually exclusive outputs. (C) The maximum and the average fitness scores for the top 50% best-fit topologies in our genetic algorithm as a function of the generation number. After roughly 30 generations the genetic algorithm returns a stable configuration. (D) Example of a more complex signaling network with multilevel crosstalk exhibiting asymmetric hierarchical inhibition. The solid red line represents the dominant inhibitory link and dashed red line represents the non-dominant inhibitory link. (E) Example of a signaling network exhibiting specificity with three inhibitory links. (F) The introduction of most feedback loops (indicated as solid blue lines) does not impair the signaling specificity. However, specific feedback loops, such as the one drawn as a dashed blue line, can comprise signaling specificity.

topology and hierarchical since one pathway exerts its inhibitory effect before the other pathway does. Remarkably, the topological asymmetry of this inhibition scheme is consistent with the functional asymmetry that requires two competing pathways respond in a mutually exclusive manner such that one pathway is dominant.

5.2.3 Generalization of our results

The lessons learned from the four-node model can be used in the analysis of more general and complex networks. In particular, the insight that asymmetric hierarchical inhibition provides a mechanism for specificity can be applied to topologies where cross-activation occurs at multiple levels. An example of such a topology is shown in Fig. 5.2D, where we have applied the coarse-graining method described before to two cross-activating pathways. In the simplest case, the nodes are linked through direct activation or cross-activation, again represented by black arrows between nodes. More complicated situations, including nodes (proteins) linked through scaffolding or dimerization, can also be investigated, as we will discuss later.

Our analysis starts with partitioning the signaling components for each pathway into three sets before we implement any inhibitory links. The first set contains all pathway-specific components, as enclosed in the solid box in Fig. 5.2D. Since these components are not affected by crosstalk but solely controlled by the input signal, we will refer to this set as the input set. The second set, drawn within the dashed-dotted box, contains components that are downstream from the input set and upstream from the last component in the cascade affected by cross-talk. This intermediate set may involve many cross-activation links, and it is important to recognize that signaling specificity is not measured at this level. The third and final set is drawn within the dashed box and named the output set, as it includes the last component subject to cross-activation, along with all its downstream nodes. Obviously, signaling specificity has to be achieved at this output level, regardless of the cross-activation dynamics within the intermediate sets.

The asymmetric hierarchical inhibition mechanism discovered in the analysis of the four-node module suggests that adding two inhibitory links is sufficient to achieve signaling specificity here. One of these links describes the inhibition exerted by one component from the input set of the dominant pathway (assumed to be the X pathway here) on another component in the output set of the non-dominant pathway. We refer to this link as the dominant inhibitory link hereafter. The second link, also called the non-dominant inhibitory link, represents the inhibition of an output-set component in the X pathway by either the Y-pathway component receiving the dominant inhibition or any of its downstream nodes.

Unlike the simple four-node topology in Fig. 5.2, there is generally no longer a unique way to place the inhibitory links. The number of possible topologies, however, can be easily enumerated. Let m_1 and n_1 (m_2 and n_2) be the number of components in the input and output sets of pathway X (pathway Y), respectively. Then, the number of ways, N, that we can organize the inhibitory links is given by

$$N = m_1 \sum_{j=1}^{n_2} (n_2 - j + 1) n_1 = \frac{1}{2} m_1 n_1 n_2 (n_2 + 1). \tag{5.1}$$

We can compare N to the total number of possible topologies that involve just two inhibitory links, with one link connecting X to Y and the other connecting Y to X. If the intermediate sets are not considered in the enumeration, this total number is $N_{tot} = (m_1 + n_1)^2 (m_2 + n_2)^2$. One can see that the topologies based on asymmetric hierarchical inhibition constitute a small fraction in the entire topology space, especially when the number of components in the first and third sets is large. We have verified numerically that these topologies are the ones that generate signaling specificity.

The discussion above is limited to the case of two inhibitory links. Additional links, however, can be easily incorporated. The enumeration of topologies is still possible but might now involve the number of components in the intermediate sets. Clearly, adding more inhibitory links increases the number of possible combinations. Fig. 5.2E illustrates an example of the topology that exhibits specificity through three inhibitory links. The most upstream inhibitory link creates an input-specific component in the intermediate set of the dominant pathway. This

component in turn inhibits a component in the output set of the non-dominant pathway. As before, a non-dominant link is required to ensure signaling specificity when pathway Y is activated.

Finally, the topology in Fig. 5.2D only contains feedforward links. The addition of feedback loops can be analyzed in a straightforward manner. Examples of these loops are shown in Fig. 5.2F as blue lines. It is easy to verify that the feedback loops, indicated by solid blue links, do not interfere with the pathway specificity. Specificity can be impaired, however, if the feedback loop links a non-specific component to a pathway-specific node that has direct or indirect control on the dominant inhibitory link. An example of such a feedback loop is shown as the dashed blue line in Fig. 5.2F.

5.2.4 Application to yeast signaling pathways

We will now apply our analysis to the yeast cell *Saccharomyces cerevisiae*, where a common set of protein kinases are activated in both the mating process and the filamentous growth response [3, 14, 15]. The mating program is initiated by the binding of pheromones to G protein-coupled receptors on the cell membrane. This triggers the dissociation of G protein into two subunits: G_α and $G_{\beta\gamma}$. The latter recruits the scaffold protein Ste5 to the membrane that co-localizes and activates in order the MAPK kinase kinase (MAPKKK) Ste11, the MAPK kinase (MAPKK) Ste7, and the MAPK Fus3. Several upstream kinases, including Ste20 and Ste50, also facilitate this sequential reaction. The MAPK Fus3 is a mating-specific component that not only controls mating gene expression but also promotes the cell cycle arrest and the morphological projection toward the mating partner. In particular, Fus3 activates the transcription factor Ste12 in the nucleus by phosphorylating Ste12 inhibitors, Dig1 and Dig2. As a result, activated Ste12 bind cooperatively to the promoters of mating genes and drive their expression.

The switch to a filamentous growth form in yeast is triggered under the starvation of certain nutrients [3]. This filamentation pathway is mediated by a MAPK module that shares the MAPKKK Ste11 and MAPKK Ste7 with the mating pathway. The MAPK of the filamentation pathway is Kss1, which is highly homologous

to Fus3 and which activates Ste12 as well as a filamentation-specific transcription factor Tec1. Cooperative binding of active Ste12 and Tec1 at the promoters drives the expression of filamentation genes. Remarkably, active Fus3 suppresses Tec1 by accelerating its degradation and thus prevents the crosstalk with the filamentation genes [16, 17]. This strong inhibition is irreversible and makes the mating pathway dominant in competition with the filamentation pathway. Without its negative regulatory property, Fus3 appears functionally redundant with Kss1 [16]. Finally, both the mating and filamentation pathways have genetic positive feedback loops, as both Ste12 and Tec1 upregulate themselves [18].

A variety of mechanisms have been proposed and studied to explain the signaling specificity in yeast cells, including the sequestration of shared components by scaffold proteins [19, 20], the experimental identification of Fus3-dependent inhibition of Tec1 [16, 17], and the resource draining of Ste12 by Tec1 binding [10, 21] and Ste12-Tec1 degradation [11]. Since there is no absolute physical separation of the MAPK-dependent signaling cascades, cross-pathway inhibition is the likely solution to promote signaling specificity.

A graphical representation of the yeast mating and filamentation pathways is shown in Fig. 5.3A, where some of the nodes are not connected through a direct activation link. For example, the activation of Fus3 requires the scaffold protein Ste5 that coordinates the MAPK cascade; also, the formation of the Ste12-Ste12 or Ste12-Tec1 dimers relies on the activation of Ste12 first. Nevertheless, such subtle dependence can still be treated as activation links since they represent causal relationships between the nodes. By the coarse-graining techniques described before, the original network in Fig. 5.3A can be reduced to the graph in Fig. 5.3B, which contains a minimal set of nodes and links that capture the skeleton underlying the full topology. We have also identified the input, intermediate and output sets in the same figure. For example, Fus3 is part of the input set of the mating pathway, since its activation depends on the mating-specific protein Ste5. The filamentation MAPK Kss1, in contrast, is nonspecific because it is activated in both pathways. Furthermore, Kss1 is not the most downstream component being cross-activated, and thus belongs to the intermediate set of the filamentation pathway.

In summary, the input set of the mating pathway contains Fus3, Ste5 and a node representing all the mating-specific components (e.g., the G-protein) upstream of Ste5. Its intermediate set is empty, whereas the output set consists of both Ste12 and Ste12-Ste12. The filamentation pathway, on the other hand, has an undefined input set because its input-specific components are not clearly identified so far. It has an intermediate set which contains only Kss1 and an output set that is made up of Tec1 and Ste12-Tec1.

The above partitioning implies that $m_1 = 3$, $n_1 = 2$ and $n_2 = 2$. Then, by Eq. 5.1, we can enumerate 18 ways to place two inhibitory links upon the reduced topology, such that it restores signaling specificity and makes the mating pathway dominant. Although the input set of the mating pathway contains several nodes, the dominant inhibitory link is unlikely to originate from an upstream component (e.g., Ste5) other than Fus3. This is because experiments have identified a Fus3 mutant that is defective in suppressing Tec1 and causes crosstalk [16, 17]. Thus, we will focus here on those topologies with the dominant inhibitory link originating from Fus3. Such restriction leads to the six possible topologies in Fig. 5.3C.

Of the six topologies we have shown, only two appear to be consistent with existing experimental data. Topology 1, involving the non-dominant inhibition of Ste12 by Tec1, turns to be implausible, because the activity of Ste12 is requisite for the formation of Ste12-Tec1 in the filamentation pathway [3, 18]. Topology 2 and 4 involve the inhibition of mating genes by Ste12-Tec1. Experiments, however, indicate that Ste12-Tec1 binds specifically to the promoters of filamentation genes [18], making such inhibition unlikely. Of course, there remains the possibility that some of the filamentation gene products suppress the mating gene transcription, though this requires faster expression of filamentation products than that of mating products. The dominant inhibitory link in topology 3 and 4 comes from the direct inhibition of Ste12-Tec1 by Fus3 or the blocking of promoter sites for the filamentation genes by Fus3. Again, these topologies are unappealing for lack of experimental foundation.

The two most probable topologies are number 5 and 6 in which Fus3 directly inhibits Tec1, as demonstrated in experiments [16, 17]. In topology 5, Tec1

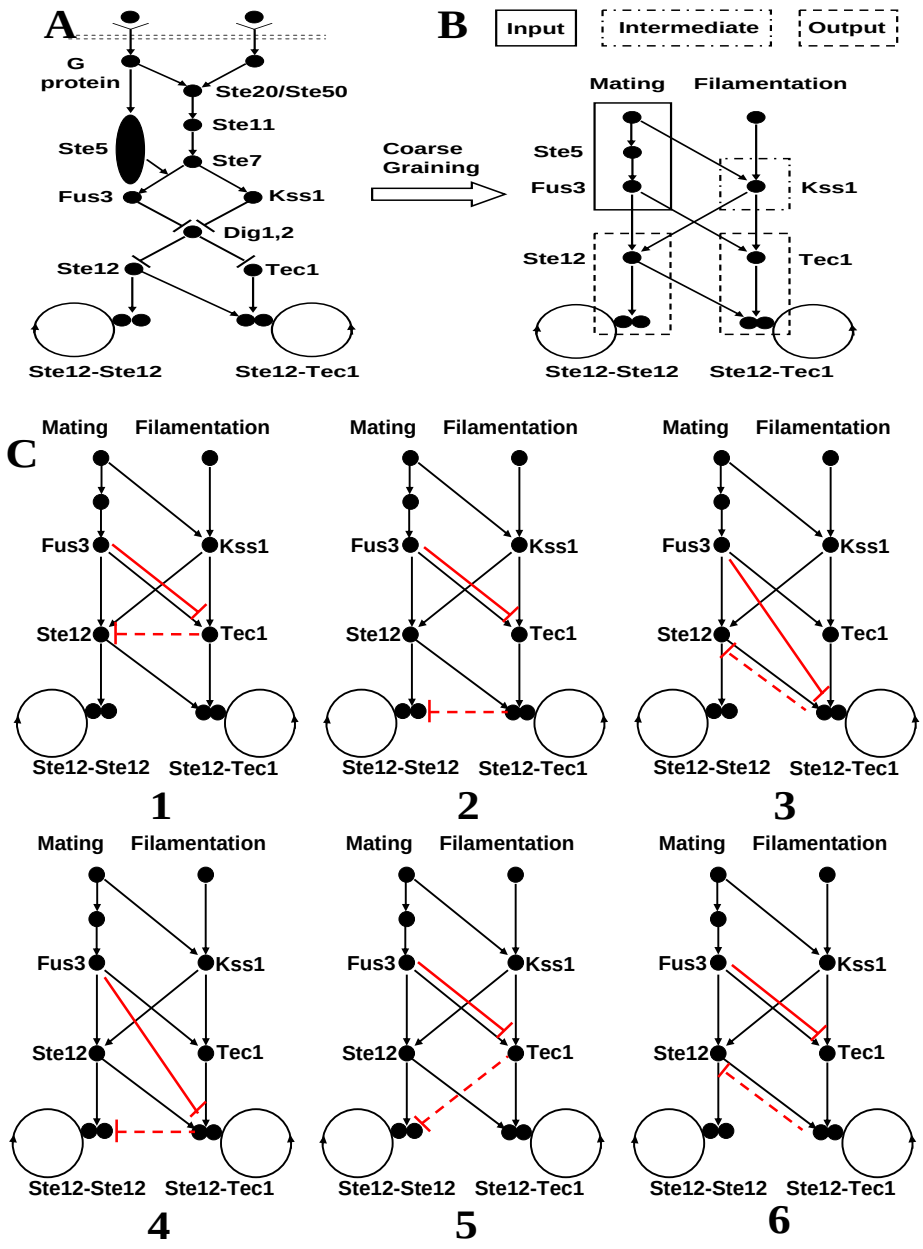


Figure 5.3: (A) The MAPK-dependent mating and filamentous growth pathways in yeast, including loops representing the feedback in gene transcription. (B) The result of coarse-graining and grouping of the components of the pathways in A. (C) All possible topologies implementing the asymmetric hierarchical inhibition mechanism. The dominant inhibitory links is shown as a solid red line while the non-dominant inhibitory link is drawn as a dashed red line. Only topology 5 and 6 are possibly consistent with existing experimental data.

may selectively suppress the formation or activity of the homodimer Ste12-Ste12. Topology 6 relies on the inhibition of Ste12 by the heterodimer Ste12-Tec1. This inhibition can be viewed as a resource depletion effect because the formation of heterodimers depletes the available Ste12 monomers [10, 11, 21]. This effect was also studied in our recent work [11], where we argued that the dimerization process alone is not sufficient but requires additional draining mechanism like the degradation of Ste12-Tec1.

5.3 Discussion

Finding network topologies that exhibit signaling specificity in the presence of shared components can, in principle, be accomplished through systematic experimental studies and careful data analysis. Such a search, however, is most likely time-consuming, especially when there is no clue or guidance. For both practical and theoretical purposes, it is useful to explore the basic design principles underlying the allowed topologies for cross-activating pathways. Such a seek for design principles in biological circuits is not limited to the problem of signaling specificity and, for example, has recently been carried out for biochemical adaptation [22].

In this study, we were able to determine a four-node module as the basic building block of cross-activating pathways (Fig. 5.1). This simple module can be analyzed easily, either by direct simulation and parameter sweeps [22, 23] or using a carefully devised genetic algorithm as we have presented. The result of this analysis shows that signaling specificity can be achieved by implementing two inhibitory links, which have to be placed at different levels of the network. The resulting inhibition scheme is classified as the asymmetric hierarchical inhibition [11], which is argued to be the general mechanism of cross-pathway inhibition to promote signaling specificity.

At first glance, it seems surprising that the genetic algorithm does not return a symmetric inhibition scheme in which the output components suppress each other. Such output mutual inhibition has been proposed as a solution for signaling specificity in several previous studies [7, 10, 24]. For cross-activation rates

that are comparable to direct activation rates, this inhibition module, however, has an intrinsic problem with the pathway specificity. For example, specificity for the X branch requires a stronger inhibition of Y_{out} by X_{out} than the other way around, which naturally compromises the specificity for the Y branch. This scheme of output reciprocal inhibition may be more applicable for the case where cross-activation is much weaker than direct activation of downstream proteins.

Our studies suggest a general approach to unravel the specificity puzzle in cross-activating signaling cascades. The first step requires the identification of those input-specific components for each pathway (i.e., the input set). The second step is to identify the output sets which are made up of the components only affected by the final cross-activation, directly or indirectly. A common feature of both the input and output sets is that there exists no internal cross-activation among their components. All the remaining nodes that are downstream of the input set but upstream from the output set fall into the intermediate set. The above classification enables us to draw a coarse-grained diagram for the original full network. By our analysis of the four-node module, we argue that the hierarchical implementation of two inhibitory links is sufficient to achieve pathway specificity. In general, the proposed asymmetric inhibition scheme only allows for a limited number of specificity-ensuring topologies, which can be enumerated easily. As the last step, these candidate topologies have to be compared with the available data or further examined in experiments. Clearly, the process described above can be much easier than starting with a detailed analysis of the full network, in particular for crosstalk pathways with a small number of pathway-specific components.

We applied this general approach to analyze the mating and filamentation pathways in *Saccharomyces cerevisiae*, a well-studied model system for crosstalk. After coarse-graining of the two pathways, we were able to classify the signaling components into the three sets based on their regulatory roles. The rule of asymmetric hierarchical inhibition suggests that the mating-specific MAPK Fus3 and the filamentation transcription factor Tec1 are key components that determine viable network structures for signaling specificity. Our analysis resulted in six candidate topologies (Fig. 5.3C), among which only the last two seem to be

compatible with experimental data. These two plausible topologies, number 5 and 6 in Fig. 5.3C, are both characterized by the dominant inhibitory link between Fus3 and Tec1, as demonstrated experimentally [16, 17]. However, they have different non-dominant inhibitory links. In topology 5, the non-dominant link between Tec1 and Ste12-Ste12 may represent the selective inhibition of Ste12-Ste12 by active Tec1, which could be an interesting hypothesis for future experimental tests. In topology 6, the non-dominant inhibition between Ste12 and Ste12-Tec1 can be accomplished by a resource draining mechanism: the formation and degradation of the heterodimer Ste12-Tec1 depletes the available Ste12 monomers such that the production of the homodimer Ste12-Ste12 is greatly suppressed. This mechanism was indeed proposed in our recent work [11], where we analyzed the yeast network through detailed simulations.

Our analysis can be extended in several ways. The current study only considered the deterministic properties of signaling pathways. It could be interesting to incorporate fluctuations inherent in the biomolecular networks and investigate the robustness of our proposed mechanism to noise. Moreover, though we have focused here on the situation where one of the pathways is dominant, we can analyze, in a similar manner, the case which allows for simultaneous activation of pathways following more than one input stimulus. Finally, we have restricted ourselves throughout to two parallel pathways. It is easy to extend our analysis to more than two pathways. An example of such an extension could be the inclusion of the high osmolarity glycerol pathway in yeast [3, 24].

5.4 Materials and Methods

5.4.1 The four-node ODE model

The basic four-node topology with cross-activation is represented by four general ordinary differential equations (ODEs) for the four variables describing the

activity of the network:

$$\frac{dX_{in}}{dt} = I_1 - [d_{xin} + g_1(Y_{in}) + g_2(Y_{out})]X_{in}, \quad (5.2)$$

$$\frac{dY_{in}}{dt} = I_2 - [d_{yin} + g_3(X_{in}) + g_4(X_{out})]Y_{in}, \quad (5.3)$$

$$\frac{dX_{out}}{dt} = -[d_{xout} + g_5(Y_{in}) + g_6(Y_{out})]X_{out} + f_1(X_{in}) + f_2(Y_{in}), \quad (5.4)$$

$$\frac{dY_{out}}{dt} = -[d_{yout} + g_7(X_{in}) + g_8(X_{out})]Y_{out} + f_3(Y_{in}) + f_4(X_{in}), \quad (5.5)$$

where $I_{1,2}$ represent the input signals and the parameters $\{d_{xin}, d_{xout}, d_{yin}, d_{yout}\}$ denote the basal degradation rates of the four components. Here, the activation and inhibition functions, f_i and g_i, are either linear, $f_i(x) = s_i x$ and $g_i(x) = k_i x$, or sigmoidal, $f_i(x) = s_i x/(x + s_{th})$ and $g_i(x) = k_i x/(x + k_{th})$. For both functional forms, the strength of each link is controlled by one nonnegative parameter, k_i or s_i, for $i = 1, 2, ..., 8$. The parameters s_{th} and k_{th} determine the threshold values of the inhibition and activation effects.

5.4.2 The network genetic algorithm

A network version of genetic algorithm is designed to search for optimal topologies for certain functional goal [12, 13]. Based on our four-node ODE model, the algorithm starts from a population of random realizations of the eight strength parameters $\{k_1, k_2, ..., k_8\}$. For every realized topology, we use Matlab 7.0 to solve the corresponding ODEs under three different input conditions: (a) $I_1 = 1$ and $I_2 = 0$; (b) $I_1 = 0$ and $I_2 = 1$; (c) $I_1 = I_2 = 1$. The steady-state solutions are then used to evaluate a fitness score, defined as $F = w(S_X + S_Y + C_{XY}) - \sum_{i=1}^{8} k_i$, which measures the functional performance of a realized topology. Here, we have introduced two metrics for signaling specificity (S_X and S_Y) [7, 25] and one metric for pathway dominance (C_{XY}); they are $S_X = \log(X_{out}/Y_{out})$ under condition (a), $S_Y = \log(Y_{out}/X_{out})$ under condition (b), and $C_{XY} = \log(X_{out}/Y_{out})$ under condition (c). To filter out dispensable links, the fitness function also incorporates a cost term represented by the total strength of all the inhibitory links, $\sum_{i=1}^{8} k_i$. To further balance cost and performance, a weight parameter w was found to be helpful.

All parameters are fixed throughout except $\{k_1, k_2, ..., k_8\}$ which are allowed to vary independently in the space $[0, k_{max1}] \times [0, k_{max2}] ... \times [0, k_{max8}]$. The simulation is started using 1000 topologies with randomly chosen values of k_i. The algorithm then sorts all the topologies based on their fitness scores. A fixed fraction (e.g. 50%) of best-fit topologies are kept as seed configurations for reproduction in the next generation, where the parameters $\{k_1, k_2, ..., k_8\}$ encoding every seed are subject to random mutation, that is, increasing or decreasing each k_i by a small amount δk with equal probability. We repeat the procedure by evaluating the fitness scores for the newly generated topologies and selecting the top 50% best-fit ones as seeds for another round of reproduction. To monitor the process, we calculate the average fitness for the top 50% networks. The algorithm stops when it reaches a stable average fitness value. We expect that the optimal network solutions are encoded by the parameters $\{k_1, k_2, ..., k_8\}$ that correspond to this stable fitness value. For the case where Pathway X is dominant, the algorithm returns a unique solution $\{k_1, k_2, ..., k_8\}^* = \{0, 0, 0, 0, 0, +, +, 0\}$, corresponding to the scheme of asymmetric hierarchical inhibition in Fig. 5.2B. We have verified that this solution is independent on the specific choice of the parameter values or on the functional forms of the biochemical interactions. The above genetic algorithm is generally applicable to more complex signaling networks. One possible implementation is to screen out the candidate inhibitory links in the yeast MAPK signaling system.

5.5 Acknowledgements

Chapter 5, in part, is the published material as it appears in Physical Biology, (2011), Hu, Bo; Levine, Herbert; Rappel, Wouter-Jan. The dissertation author was the primary investigator and author of this paper.

Bibliography

[1] M.A. Schwartz and V. Baron, Curr. Opin. Cell Biol. **11**, 197 (1999).

[2] M.A. White and R.G. Anderson, Annu. Rev. Pharmacol. Toxicol. **45**, 587 (2005).

[3] M.A. Schwartz MA and H.D. Madhani, Annu. Rev. Genet. **38**, 725 (2004).

[4] R. Seger and E.G. Krebs, FASEB J. **9**, 726 (1995).

[5] L. Chang L and M. Karin, Nature **410**, 37 (2001).

[6] P.J. Stork and J.M. Schmitt, Trends Cell Biol. **12**, 258 (2002).

[7] L. Bardwell, X. Zou, Q. Nie, and N.L. Komarova, Biophys. J. **92**, 3425 (2007).

[8] W. Chen, H. Levine, and W.J. Rappel, Phys. Biol. **5**, 046006 (2008).

[9] W. Chen, H. Levine, and W.J. Rappel, Phys. Rev. E **80**, 041901 (2009).

[10] M.N. McClean, A. Mody, J.R. Broach, and S. Ramanathan, Nat. Genet. **39**, 409 (2007).

[11] B. Hu, W.J. Rappel, and H. Levine, Biophys. J. **96**, 4755 (2009).

[12] P. François and V. Hakim, Proc. Natl. Acad. Sci. U.S.A. **101**, 580 (2004).

[13] P. François, V. Hakim, and E.D. Siggia, Mol. Syst. Biol. **3**, 154 (2007).

[14] H. Liu, C.A. Styles, and G.R. Fink, Science **262**, 1741 (1993).

[15] R.L. Roberts and G.R. Fink, Genes Dev. **8**, 2974 (1994).

[16] S. Chou, L. Huang, and H. Liu, Cell **119**, 981 (2004).

[17] M.Z. Bao, M.A. Schwartz, G.T. Cantin, J..R 3rd Yates, and H.D. Madhani, Cell **119**, 991 (2004).

[18] J. Zeitlinger, I. Simon, C.T. Harbison, N.M. Hannett, T.L. Volkert, G.R. Fink, and R.A. Young, Cell **113**, 395 (2003).

[19] L.J. Flatauer, S.F. Zadeh, and L. Bardwell, Mol. Cell Biol. **25**, 1793 (2005).

[20] M. Good, G. Tang, J. Singleton, A. Reményi, and W.A. Lim, Cell **136**, 1085 (2009).

[21] S. Chou, S. Zhao, Y. Song, H. Liu, and Q. Nie, Mol. Syst. Biol. **4**, 212 (2008).

[22] W. Ma, A. Trusina, H. El-Samad, W.A. Lim, and C. Tang, Cell **138**, 760 (2009).

[23] W. Ma, L. Lai, Q. Ouyang, and C. Tang, Mol. Syst. Biol. **2**, 70 (2006).

[24] H.Y. Yang, K. Tatebayashi, K. Yamamoto, and H. Saito, EMBO J. **28**, 1380 (2009).

[25] N.L. Komarova, X. Zou, Q. Nie, and L. Bardwell, Mol. Syst. Biol. **1**, 23 (2005).